RSC Advances

PAPER

View Article Online
View Journal | View Issue



Cite this: *RSC Adv.*, 2026, **16**, 819

# Piperidine-catalyzed synthesis of (*E*)-2-cyanoacrylamides: crystallographic, antiproliferative, and docking studies

Camilo Serrano-Sterling,[a] Isabel Iriepa,[bc] Mario A. Macías,[d] Juan-Carlos Castillo *[a] and Diana Becerra*[a]

A piperidine-catalyzed Knoevenagel condensation between (hetero)aromatic aldehydes **1a–i** and 2-cyanoacetamide **2a** was developed to afford (*E*)-2-cyano-3-(het)arylacrylamides **3a–i** in 40–95% yields under mild and environmentally friendly conditions. The methodology was further extended to other methylene active compounds, including malonamide **2b** and ethyl cyanoacetate **2c**, providing the corresponding adducts **3m–o** in 54–81% yields. The (*E*)-stereochemistry of 3-arylacrylamide **3i** was unambiguously confirmed by single-crystal X-ray diffraction analysis. The antiproliferative activity of compounds **3a–o** was evaluated across the NCI-60 human cancer cell line panel. Compounds **3f** and **3o** exhibited the highest potency against the CAKI-1 renal cancer cell line, with $GI_{50}$ values of 0.287 μM and 0.336 μM, respectively, while compound **3n** showed its strongest activity against the RPMI-8226 melanoma cell line ($GI_{50}$ = 0.367 μM). These values are comparable to or lower than those of the reference drug Osimertinib ($GI_{50}$ = 0.343 μM for CAKI-1 and 1.95 μM for RPMI-8226 cell lines). In all active cases, $LC_{50}$ to $GI_{50}$ ratios equal to or greater than 100 indicated selective growth inhibition rather than nonspecific cytotoxicity. Compound **3n** exhibited a slightly higher cytotoxic response compared with its structural analogues. To rationalize this behavior, toxicity profiling revealed a coordinated activation of Nrf2-mediated oxidative stress, p53-dependent DNA damage response, and androgen receptor (AR-LBD) signaling pathways. Molecular docking studies further demonstrated favorable binding interactions of compounds **3f**, **3n**, and **3o** within the tyrosine kinase domain of the epidermal growth factor receptor (EGFR), with predicted affinities surpassing that of Erlotinib.

Received 19th September 2025
Accepted 12th December 2025

DOI: 10.1039/d5ra07121f

rsc.li/rsc-advances



## 1 Introduction

Covalent fragment-based drug discovery has become a central strategy in modern drug development.[1–5] Targeted covalent inhibitors (TCIs) combine a noncovalent scaffold, which ensures selective target recognition, with a reactive warhead capable of forming reversible or irreversible covalent bonds with specific amino acid residues.[6,7] Approximately 36% of these warheads are designed to target cysteine due to its low abundance in the proteome and high nucleophilic reactivity.[8] TICs offer several advantages, including enhanced potency and selectivity, prolonged duration of action, lower dosing frequency, and a lower risk of drug resistance.[1,4] However, potential drawbacks include off-target effects, immunogenicity, and dose-limiting systemic toxicity.[9,10] Advances in understanding their mechanisms of action and warhead reactivity have driven the development of multiple drug candidates and several FDA-approved therapies.[5,11–13]

Since 2001, the US FDA has approved 45 drugs that form irreversible covalent bonds with their target proteins,[14] including 11 tyrosine kinase inhibitors (TKIs) for cancer treatment (Fig. 1).[11,12] Of these, 10 feature an acrylamide moiety as the warhead, enabling covalent bond formation with target enzymes *via* a Michael addition.[15] Representative examples include Afatinib,[16] Osimertinib,[17] Dacomitinib,[18] Mobocertinib,[19] and Lazertinib,[20] which covalently bind to the thiol group of Cys797, thereby inhibiting the mutant epidermal growth factor receptor (EGFR) in non-small cell lung cancer (NSCLC).[12,13] Neratinib targets human epidermal growth factor receptor 2 (HER2) *via* covalent binding to Cys805 and is approved for HER2-positive breast cancer.[21]

Other clinically relevant TCIs include Ibrutinib, Acalabrutinib, and Zanubrutinib, which inhibit Bruton's Tyrosine Kinase (BTK) and are indicated for mantle cell lymphoma, chronic lymphocytic leukemia (CLL), small lymphocytic lymphoma

[a]*Escuela de Ciencias Químicas, Universidad Pedagógica y Tecnológica de Colombia, Avenida Central del Norte 39–115, Tunja 150003, Colombia. E-mail: juan.castillo06@uptc.edu.co; diana.becerra08@uptc.edu.co*

[b]*Departamento de Química Orgánica y Química Inorgánica, Universidad de Alcalá, Ctra. Madrid-Barcelona, km. 33, 6, 28871 Madrid, Spain*

[c]*Institute of Chemical Research Andrés M. del Río, Universidad de Alcalá, Alcalá de Henares, 28805 Madrid, Spain*

[d]*Cristalografía y Química de Materiales, Departamento de Química, Universidad de los Andes, Carrera 1 No. 18A–10, Bogotá 111711, Colombia*

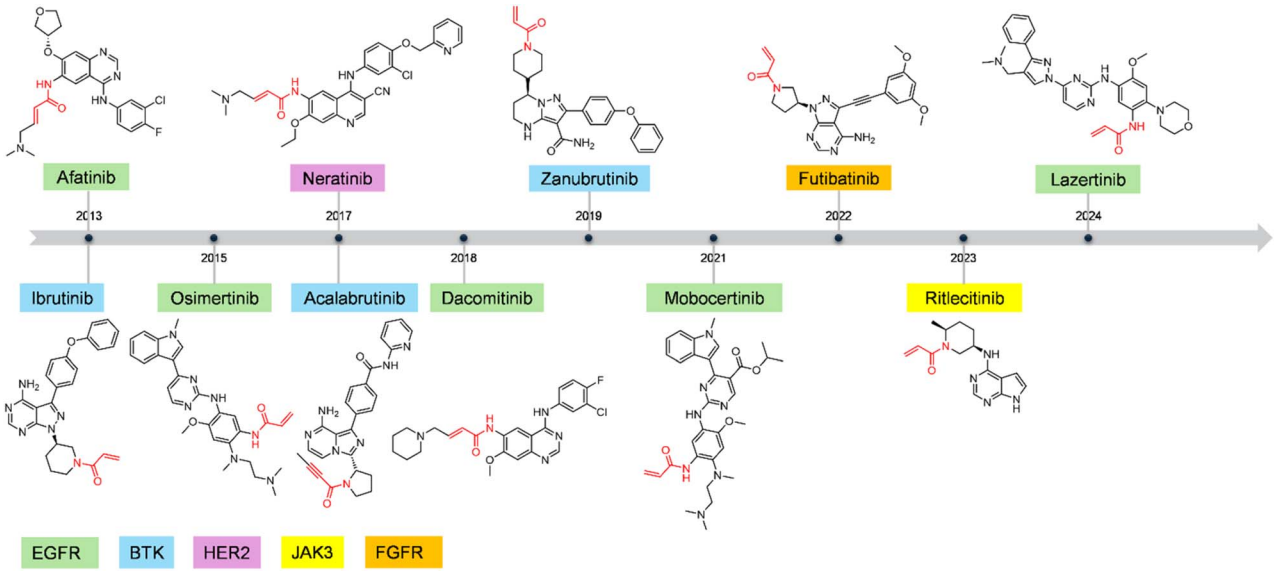


Fig. 1 FDA-approved irreversible tyrosine kinase inhibitors (TKIs) for cancer treatment.

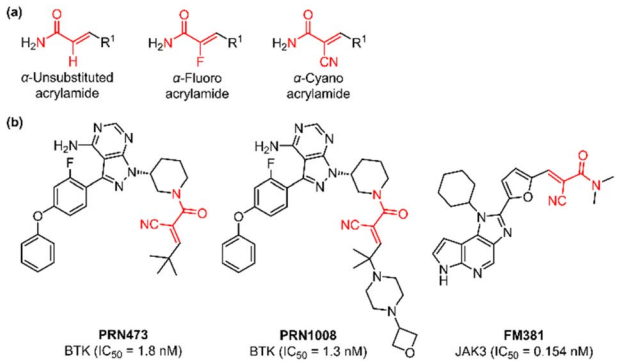


Fig. 2 (a) Classification of acrylamide-based warheads, and (b) applications of α-cyanoacrylamides in BTK inhibitors.

(SLL), and marginal zone lymphoma.[22–24] Futibatinib targets fibroblast growth factor receptors 1–4 (FGFR1–4) in patients with advanced intrahepatic cholangiocarcinoma harboring FGFR2 gene fusions or rearrangements,[25] while Ritlecitinib selectively inhibits Janus kinase 3 (JAK3) for the treatment of alopecia areata.[26] Finally, Lazertinib is also indicated for locally advanced or metastatic NSCLC harboring an EGFR exon 19 deletion or an exon 21 L858R substitution mutation.[12]

Based on their α-substituents, acrylamide-based warheads are categorized into α-unsubstituted, α-fluoro, and α-cyano derivatives (Fig. 2a).[15] Introduced in the 1990s, α-unsubstituted acrylamides can enhance inhibitor activity and overcome resistance but carry significant risks, including severe off-target effects and irreversible inhibition.[15] In contrast, α-cyanoacrylamides offer notable advantages, such reduced reactivity and the ability to form reversible covalent bonds with cysteine, thereby improving target selectivity and minimizing adverse effects.[27] In 2022, Owens and colleagues reported PRN473 and PRN1008 as reversible covalent BTK inhibitors, with $IC_{50}$ values of 1.8 nM and 1.3 nM, respectively (Fig. 2b).[28] In 2016, Forster and coworkers described FM381 as a reversible covalent JAK3 inhibitor, exhibiting an $IC_{50}$ value of 0.154 nM (Fig. 2b).[29]

Notably, PRN1008 and FM381 form reversible covalent bonds with Cys481 and Cys909, respectively, through their α-cyanoacrylamide warheads. These findings underscore that incorporating a α-cyanoacrylamide-based warhead can facilitate the development of novel TKIs.

Traditional synthetic routes to α-cyanoacrylamides typically involve a Knoevenagel condensation between an aldehyde and 2-cyanoacetamide in the presence of a Brønsted base.[30] In recent decades, both homogenous and heterogenous catalytic strategies have been successfully developed to improve this transformation.[30,31] Among them, metal-free catalysis has been extensively explored using readily available Brønsted bases such as triethylamine,[32] 4-methylpiperidine,[33] piperazine,[33] 1-methylpiperazine,[34] ammonium acetate,[35] and sodium hydroxide.[36] The use of piperidine under reflux in ethanol has also been documented.[37,38] Moreover, innovative approaches employing 1-methyl-3-butyl imidazolium bicarbonate as an ionic liquid and microwave-assisted heating have emerged as notable alternatives.[36,39] In our previous work, we reported the application of biogenic carbonates and functionalized hydrotalcites as efficient heterogenous catalysts for the solvent-free synthesis of α-cyanoacrylamides.[40,41] Despite these advances, current methodologies still suffer from the use of hazardous catalysts or solvents, complex catalyst preparation, high catalyst loadings, and labor-intensive purification, which limit scalability and sustainability.

This study overcomes these limitations by developing a water-promoted synthesis of α-cyanoacrylamides *via* a piperidine-catalyzed Knoevenagel condensation between (het) aromatic aldehydes and 2-cyanoacetamide at room temperature. Subsequent *in vitro* anticancer assays and molecular

docking studies demonstrated their potential as promising EGFR inhibitors in medicinal chemistry.

## 2 Results and discussion

### 2.1 Chemistry

We initiated the investigation of an efficient and straightforward approach to synthesize (*E*)-2-cyano-3-arylacrylamide **3a** through a model Knoevenagel reaction between 4-chlorobenzaldehyde **1a** and 2-cyanoacetamide **2a** (Table 1). Due to the significant acidity of 2-cyanoacetamide ($pK_a = 2.96$ and $pK_b = 11.0$), our study began with the optimization of the base. Initially, we stirred a stoichiometric mixture of 4-chlorobenzaldehyde **1a** and 2-cyanoacetamide **2a** in ethanol at room temperature for 3 h without adding a base (Entry 1, Table 1). TLC analysis showed no formation of product **3a**, highlighting the essential role of a base in this reaction. We then screened several bases using a 10 mol% catalyst loading under the same conditions. Inorganic bases, such as NaOH and KOAc, produced product **3a** in 52% and 30% yields, respectively (Entries 2 and 3, Table 1). Additionally, various organic amine bases, including triethylamine ($Et_3N$, $pK_b = 3.2$), piperidine (PP, $pK_b = 3.0$), and 1,8-diazabicyclo(5.4.0)undec-7-ene (DBU, $pK_b = 2.0$), were tested by stirring in ethanol at room temperature for 3 h (Entries 4–6, Table 1). Remarkably, piperidine delivered the most favorable result, yielding 76% of product **3a**. We attributed this higher yield to piperidine's balanced nucleophilicity, steric accessibility, and appropriate basicity, which likely contributed to its superior performance compared to $Et_3N$ and DBU. Following this, we optimized the reaction conditions by adjusting both the reaction time and solvent. Extending the reaction time to 6 h and using a 1 : 1 mixture of EtOH/$H_2O$ increased the yield of product **3a** to 85% and 89%, respectively (Entries 7 and 8, Table 1). Replacing ethanol with water alone significantly improved the yield of **3a** (93%) after stirring in water at room temperature for 6 h, using piperidine (10 mol%) as an organocatalyst (Entry 9, Table 1). However, reducing the catalyst loading to 5 mol% and extending the reaction time to 12 h resulted in lower yields of **3a** (Entries 10 and 12, Table 1).

Table 1 Optimization of the Knoevenagel synthesis of (*E*)-2-cyano-3-arylacrylamide **3a**

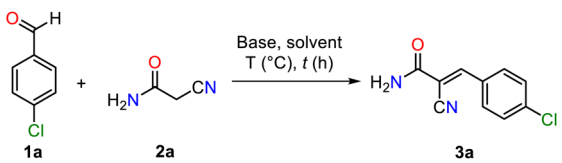


| Entry[a] | Base | mol% | Solvent | Time (h) | Yield **3a** (%) |
|---|---|---|---|---|---|
| 1 | — | — | EtOH | 3 | — |
| 2 | NaOH | 10 | EtOH | 3 | 52 |
| 3 | KOAc | 10 | EtOH | 3 | 30 |
| 4 | $Et_3N$ | 10 | EtOH | 3 | 67 |
| 5 | Piperidine | 10 | EtOH | 3 | 76 |
| 6 | DBU | 10 | EtOH | 3 | 72 |
| 7 | Piperidine | 10 | EtOH | 6 | 85 |
| 8[b] | Piperidine | 10 | EtOH/$H_2O$ | 6 | 89 |
| 9 | **Piperidine** | **10** | **$H_2O$** | **6** | **93** |
| 10 | Piperidine | 5 | $H_2O$ | 6 | 78 |
| 11 | Piperidine | 10 | $H_2O$ | 12 | 91 |
| 12 | Piperidine | 5 | $H_2O$ | 12 | 80 |

[a] Reaction conditions: **1a** (1 mmol), **2a** (1 mmol), base (5–10 mol%), solvent (3 mL), room temperature. The precipitate was filtered, washed with a cold EtOH/$H_2O$ mixture (1 : 1, v/v), and dried. [b] 1 : 1 (v/v).

With the optimized reaction conditions established, the piperidine-catalyzed Knoevenagel condensation was applied to structurally diverse (hetero)aromatic aldehydes **1a–l** and 2-cyanoacetamide **2a** to synthesize (*E*)-2-cyano-3-(het)arylacrylamides (Scheme 1). Aromatic aldehydes bearing electron-withdrawing substituents, such as 4-bromo and 4-nitro, furnished compounds **3b** and **3c** in 87% and 67% yields, respectively, after reaction times of 6 h and 24 h. Likewise, substrates containing 2,4-dichlorophenyl and 4-chloro-3-nitrophenyl moieties provided products **3d** and **3e** in good yields within 6 h. In contrast, aldehydes bearing electron-donating groups, such as 4-diphenylamino, 4-methyl, 4-methoxy, 4-hydroxyl, and 4-dimethylamino, required longer reaction times (6–24 h) and generally gave lower yields (54–88%) of products **3f–j**. This outcome can be attributed to the diminished electrophilicity of the carbonyl carbon, which reduces its susceptibility to nucleophilic attack during the Knoevenagel condensation. Notably, 9-anthraldehyde, a substrate containing an extended polycyclic aromatic system, afforded compound **3k** in 85% yield after 24 h, suggesting the tolerance of the reaction toward bulky aromatic frameworks. Finally, the heteroaromatic substrate 5-(hydroxymethyl)furfural delivered compound **3l** in 40% yield after 12 h. In all cases, the (*E*)-2-cyano-3-(het)arylacrylamides were efficiently purified by simple filtration followed by washing with a cold EtOH/$H_2O$ mixture. The (*E*)-stereochemistry of compound **3i** was unambiguously confirmed by single-crystal X-ray diffraction analysis.

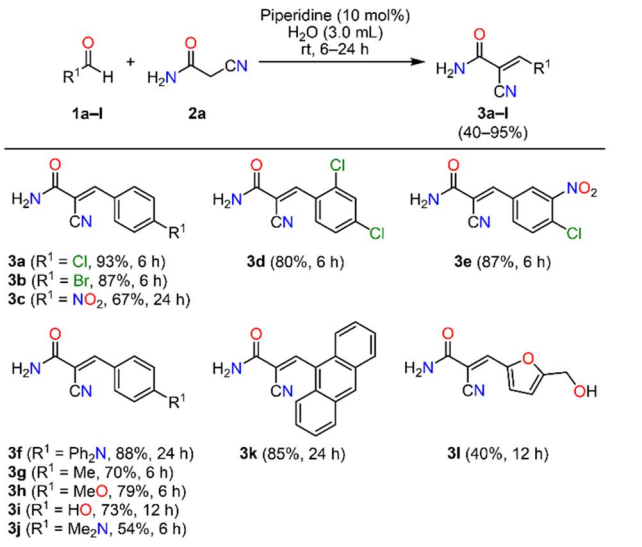


Scheme 1 Piperidine-catalyzed Knoevenagel synthesis of (*E*)-2-cyano-3-(het)arylacrylamides **3a–l**.

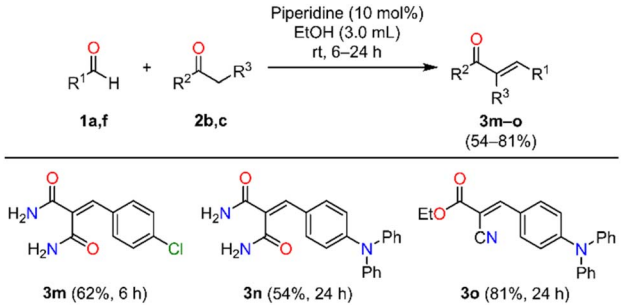


Scheme 2 Piperidine-catalyzed synthesis of Knoevenagel adducts 3m–o.

Subsequently, the piperidine-catalyzed Knoevenagel protocol was extended to other methylene active compounds, such as malonamide **2b** and ethyl cyanoacetate **2c** (Scheme 2). Preliminary experiments revealed that water was unsuitable as the reaction medium due to the limited solubility of the precursors, which resulted in reduced reactivity. Consequently, ethanol was selected as a sustainable alternative. The condensation of 4-chlorobenzaldehyde **1a** with malonamide **2b** in ethanol for 6 h furnished compound **3m** in 62% yield after simple filtration. Next, the protocol was applied to the less reactive 4-(diphenylamino)benzaldehyde **1f** with methylene active compounds **2b** and **2c** for 24 h, affording products **3n** and **3o** in 54% and 81% yields, respectively. Due to the high solubility of these products in ethanol, purification was performed by column chromatography on silica gel.

Finally, we performed functionalization reactions to obtain 3-arylacrylamide derivatives, given their relevance in both medicinal chemistry and chemical sensing.[42,43] Accordingly, selective *O*-alkylation of the hydroxyl group in 3-arylacrylamide **3i** was performed using propargyl bromide **4a** and cesium carbonate in DMF at room temperature for 3 h, affording the terminal alkyne **5** in 89% yield (Scheme 3). Subsequently, a copper-catalyzed azide–alkyne cycloaddition (CuAAC) was performed using *O*-propargylated 3-arylacrylamide **5**, benzyl bromide **4b**, and sodium azide in the presence of CuI (10 mol%) as the catalyst in a mixture of ethanol and water at 60 °C for 12 h, affording the 1,4-disubstituted 1,2,3-triazole **6** in 79% yield. Notably, this multicomponent transformation enabled

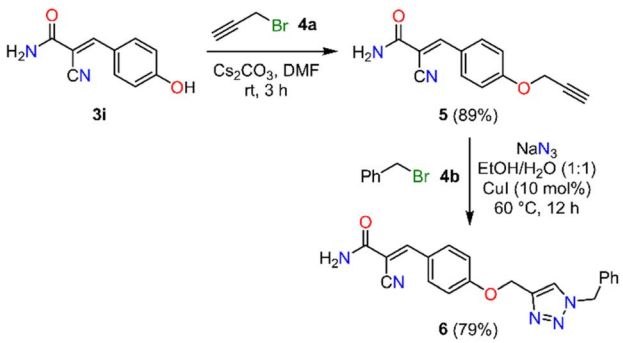


Scheme 3 Functionalization reactions of (*E*)-2-cyano-3-(4-hydroxyphenyl)acrylamide **3i**.

the formation of three C–N bonds in a single step, employing an eco-friendly solvent and proceeding under ligand-free conditions.

### 2.2 FT-IR and NMR spectroscopy studies

The solid-state FT-IR spectra of the Knoevenagel adducts **3a–o** exhibited characteristic absorption bands consistent with the functional groups anticipated in their proposed molecular structures (Fig. S2–S7 in SI). For compounds **3a–n**, the asymmetric and symmetric N–H stretching vibrations of non-hydrogen-bonded groups were observed in the ranges 3362–3455 $cm^{-1}$ and 3302–3373 $cm^{-1}$, respectively. Additional absorption bands at 3236–3288 $cm^{-1}$ and 3151–3193 $cm^{-1}$ were assigned to the asymmetric and symmetric hydrogen-bonded N–H stretching vibrations. The amide C=O stretching vibration appeared in the range 1652–1715 $cm^{-1}$ for compounds **3a–n**, while compound **3o** exhibited an ester C=O stretching vibration at 1711 $cm^{-1}$. Finally, the C≡N stretching vibration was detected in the range of 2200–2230 $cm^{-1}$ in compounds **3a–l** and **3o**.

Further structural elucidation was performed using $^{1}H$ and $^{13}C$ NMR spectroscopy in DMSO-$d_6$ and $CDCl_3$ (Fig. S8–S24 in SI). The (*E*)-2-cyano-3-(het)arylacrylamides **3a–l** and **3o** exhibited a characteristic singlet in the range of $\delta$ 7.93–9.07 ppm, attributable to the H-3 proton. The $^{13}C$ NMR spectra confirmed the presence of the C-3 carbon ($\delta$ 135.9–150.5 ppm) and the carbonyl carbon of the acrylamide moiety ($\delta$ 161.6–164.0 ppm). In the Knoevenagel adducts **3m–o**, the $\beta$-proton and $\beta$-carbon appeared in the ranges of $\delta$ 7.28–8.09 ppm and $\delta$ 132.8–154.1 ppm, respectively, reflecting the electronic effects of the substituents on the conjugated aryl system. Moreover, the ester carbonyl in compound **3o** was observed at $\delta$ 163.8 ppm, while compounds **3m** and **3n** exhibited two distinct amide carbonyl signals in the range of $\delta$ 165.6–169.6 ppm, indicative of non-equivalent amide environments.

### 2.3 X-ray crystallographic studies

The crystal structure of compound **3i** was determined by single-crystal X-ray diffraction (Table S18 shows the crystallographic data). Fig. 3a shows the ORTEP representation of **3i**, illustrating its nearly planar conformation with only a slight distortion at the carbonyl group, most likely resulting from packing effects.

The electrostatic potentials (EPSs) mapped on the Hirshfeld surface (calculated at the B3LYP level with the 6-31G(d,p) basis set) indicate that the most electronegative and electropositive regions are localized on the carbonyl/cyano and hydroxyl/amino groups, respectively (Fig. 3b). Consistently, the strongest hydrogen bond is formed between the hydroxyl group (donor) and the carbonyl group (acceptor) (Fig. 3c). These hydrogen bonds are complemented by short N–H···N and N–H···O non-covalent interactions involving the amino (donor) and hydroxyl (acceptor) groups, leading to the formation of molecular layers stabilized by π···π stacking interactions and van der Waals forces (Fig. 3d). The resulting supramolecular structure displays layered architecture, with strong interactions holding the sheets together and weaker interactions operating in the

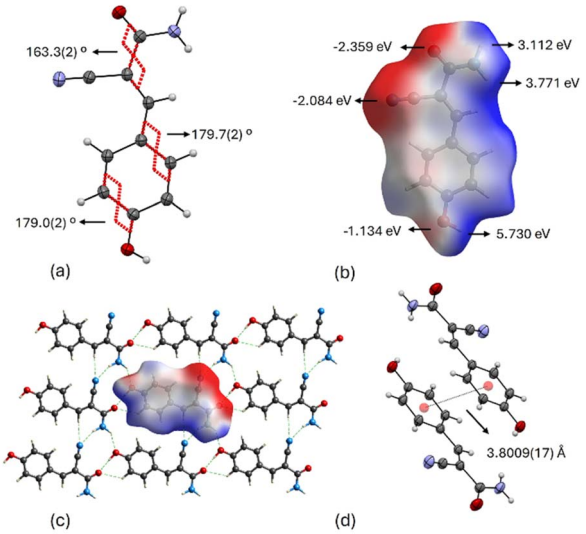


Fig. 3 (a) Molecular structure of **3i** with anisotropic thermal vibration ellipsoids drawn at the 30% probability level. Hydrogen atoms are represented as spheres of arbitrary radius. (b) Electrostatic potentials (ESPs) mapped on Hirshfeld surfaces in the range −0.05 a.u. (red), through zero (white), to 0.05 a.u. (blue) for **3i**. (c) Hydrogen bonding of **3i** forming molecular sheets. (d) π···π interactions connecting the sheets. The crystallographic information file (CIF) has been deposited in the Cambridge Crystallographic Data Center under deposition number CCDC-2483802. The compound crystallizes in the triclinic space group $P\bar{1}$, with unit cell parameters $a = 6.7404(17)$ Å, $b = 7.146(2)$ Å, $c = 10.511(2)$ Å, $\alpha = 105.94(2)°$, $\beta = 97.682(19)°$, $\gamma = 111.43(3)°$, and $Z = 2$ with $Z' = 1$.

interlayer zone. Detailed crystallographic data (Table S18), hydrogen-bonding parameters (Table S19), bond lengths (Table S22), bond/valence angles (Table S23), and torsion/dihedral angles (Table S24) are provided in the SI.

After extensive attempts to optimize the crystallization conditions, low-quality crystals of compound **3n** were obtained and subjected to X-ray data collection. Although the diffraction data yielded suboptimal statistical parameters, they were sufficient to confirm the molecular structure (Table S20). Due to low-quality data, the CIF file was not deposited in the CCDC; however, the file, including the embedded HKL data, has been provided in the SI. According to these data, compound **3n** crystallizes in the triclinic space group *P*-1 with unit cell parameters $a = 9.1161(13)$ Å, $b = 11.3530(12)$ Å, $c = 21.0258(17)$ Å, $\alpha = 99.481(8)°$, $\beta = 95.989(10)°$, $\gamma = 102.881(11)°$, and $Z = 2$ with $Z' = 1$. In the supramolecular structure, the 2-methylenemalonamide fragment promotes short C–H···O and N–H···N hydrogen bonds that assemble into molecular sheets stacked along the *c* axis, further connected through the *N*,*N*-diphenylaniline fragment by C–H···π contacts. Detailed crystallographic data (Table S20), hydrogen-bond parameters (Table S21), the ORTEP representation, and the crystal packing (Fig. S1) are provided in the SI.

### 2.4 Physicochemical and drug-likeness profiling

To determine whether the Knoevenagel adducts **3a–o** comply with Lipinski's Rule of Five (Ro5), their physicochemical properties were analyzed using Molinspiration (Table 2). The Ro5 predicts oral bioavailability by evaluating key parameters related to aqueous solubility and membrane permeability, including molecular weight (≤500 Da), lipophilicity (log $P \leq 5$), hydrogen bond donors (≤5), and hydrogen bond acceptors (≤10).[44] Among the series, only compound **3o** exceeded the recommended log *P*, with a value of 6.12. This deviation results from the replacement of the primary amide (–$CONH_2$) in the α-cyanoacrylamide core with an ethyl ester (–COOEt), eliminating a hydrogen-bond donor, combined with the presence of an *N*,*N*-diphenylamino group that extends the aromatic surface. These features reduce polarity, increase hydrophobic bulk, and promote partitioning into nonpolar phases, explaining the elevated log *P*.

Table 2 Lipinski's parameters, fraction of $sp^3$ carbon atoms, and mean growth percentage of the tested compounds against the 60 human cancer cell lines at 10 μM

| Compound | %ABS[b] | TPSA (Å$^2$)[a] | nHBA (ON)[a] | nHBD (OHNH)[a] | log *P*[a] | MW (Da)[a] | No violations[a] | Fsp$^3$ [c]c | Mean %G[d] |
|---|---|---|---|---|---|---|---|---|---|
| **3a** | 85.92 | 66.89 | 3 | 2 | 1.80 | 206.63 | 0 | 0 | 103.28 |
| **3b** | 85.92 | 66.89 | 3 | 2 | 1.93 | 251.08 | 0 | 0 | 103.74 |
| **3c** | 70.12 | 112.71 | 6 | 2 | 1.08 | 217.18 | 0 | 0 | 103.48 |
| **3d** | 85.92 | 66.89 | 3 | 2 | 2.22 | 241.08 | 0 | 0 | 100.21 |
| **3e** | 70.12 | 112.71 | 6 | 2 | 1.68 | 251.63 | 0 | 0 | 94.54 |
| **3f** | 84.81 | 70.12 | 4 | 2 | 4.62 | 339.40 | 0 | 0 | 40.97 |
| **3g** | 85.92 | 66.89 | 3 | 2 | 1.57 | 186.21 | 0 | 0.091 | 103.65 |
| **3h** | 82.74 | 76.12 | 4 | 2 | 1.18 | 202.21 | 0 | 0.091 | 103.84 |
| **3i** | 78.95 | 87.11 | 4 | 3 | 0.64 | 188.19 | 0 | 0 | 103.04 |
| **3j** | 84.81 | 70.12 | 4 | 2 | 1.22 | 215.26 | 0 | 0.17 | 99.42 |
| **3k** | 85.92 | 66.89 | 3 | 2 | 3.23 | 272.31 | 0 | 0 | 90.54 |
| **3l** | 74.41 | 100.25 | 5 | 3 | −0.23 | 192.17 | 0 | 0.11 | 105.20 |
| **3m** | 79.26 | 86.19 | 4 | 4 | 0.74 | 224.65 | 0 | 0 | 64.54 |
| **3n** | 78.15 | 89.43 | 5 | 4 | 3.56 | 357.41 | 0 | 0 | −63.43 |
| **3o** | 90.60 | 53.34 | 4 | 0 | 6.12 | 368.44 | 1 | 0.083 | 36.80 |

[a] Values obtained from https://www.molinspiration.com. [b] %ABS = 109 − (0.345 × TPSA). [c] Fraction of $sp^3$ carbon atoms (Fsp$^3$). [d] Values obtained from the National Cancer Institute (NCI, USA).

Topological polar surface area (TPSA), a critical descriptor for predicting intestinal absorption and blood brain barrier (BBB) penetration, generally indicates that values above 140 Å$^2$ correlate with poor absorption.[45] All Knoevenagel adducts **3a–o** presented TPSA values between 53.34 Å$^2$ and 112.71 Å$^2$, remaining within the optimal range for effective absorption. Notably, compounds **3a**, **3b**, **3d**, **3g**, **3k**, and **3o** exhibited the lowest values (≤66.89 Å$^2$), with **3o** showing the minimum (53.34 Å$^2$), in line with its reduced hydrogen-bonding capacity and increased hydrophobicity.

Consistent with the TPSA trends, the estimated percentage of absorption (%ABS), a key pharmacokinetic parameter reflecting a compound's ability to permeate biological membranes,[46] ranged from 70.12% to 90.60% for compounds **3a–o**. Notably, compounds **3a**, **3b**, **3d**, **3f**, **3g**, **3h**, **3j**, **3k**, and **3o** exhibited %ABS values exceeding 80%, a feature attributable to their low TPSA (≤76.12 Å$^2$), which facilitates passive membrane permeability. Among these, compound **3o** achieved the highest absorption (90.60 Å$^2$), in line with its minimal TPSA (53.34 Å$^2$) and elevated log *P* (6.12).

The fraction of sp$^3$-hybridized carbons (Fsp$^3$) was analyzed, as this parameter is directly related to molecular three-dimensionality and can significantly influence solubility, conformational flexibility, and pharmacokinetic properties.[47] The Knoevenagel adducts **3a–o** exhibited low Fsp$^3$ values, not exceeding 0.17, consistent with predominantly unsaturated molecular frameworks. Within the series, compounds **3g**, **3h**, **3j**, **3l** and **3o** showed slightly higher Fsp$^3$ values (>0.08). Among these, **3j** reached the highest Fsp$^3$ (0.17), attributable to the *N*,*N*-dimethylamino substituent, which increases the proportion of sp$^3$-hybridized carbons.

### 2.5 Antiproliferative activity

The *in vitro* antiproliferative activity of Knoevenagel adducts **3a–o** was evaluated by the National Cancer Institute (NCI, USA). All compounds were initially subjected to a single-dose screening at 10 μM against 60 human cancer cell lines representing nine cancer panels (leukemia, melanoma, lung, colon, central nervous system, ovarian, renal, prostate, and breast) using the sulforhodamine B (SBR) assay. Results, expressed as NCI mean graphs, indicated that lower growth percentage (%G) correspond to higher growth inhibition percentage (%GI = 100 − %G), while negative %G values denote lethality (Fig. S25–S43 in SI). The mean growth percent (mean %G) represents the average of %G values across the panel of cancer cell lines; thus, mean %G ≤ 50 were considered indicative of significant active. According to this criterion, compounds **3f**, **3n**, and **3o** exhibited the highest antiproliferative activity with the mean %G of 40.97, −63.43, and 36.80, respectively, among the tested series (Table 2).[48,49]

The physicochemical and drug-likeness profiling revealed a clear correlation between antiproliferative activity and lipophilicity (Table 2). The most active compounds **3f**, **3n**, and **3o** showed high log *P* values of 4.62, 3.56, and 6.12, respectively, indicating that increased hydrophobicity enhances activity. This relationship can be rationalized by the presence of the *N*,*N*-diphenylamino substituent, which increases the aromatic surface, reduces molecular polarity, and facilitates membrane partitioning into nonpolar environments. Conversely, no consistent correlation was observed between mean %G and either topological polar surface area (TPSA) or the predicted absorption (%ABS). The structure–activity relationship (SAR) analysis derived from %GI, lethality, and mean %G data revealed two key trends: (i) incorporation of the $R^1 = NPh_2$ substituent within the α,β-unsaturated carbonyl framework of compounds **3f**, **3n**, and **3o** markedly enhances antiproliferative activity, and (ii) substitution at $R^3 = CONH_2$ in **3n** further increases activity relative to the corresponding nitrile analogues ($R^3 = CN$) in **3f** and **3o**.

Compounds **3f**, **3n**, and **3o** met the NCI selection threshold of mean %*G* ≤ 50% and were advanced to the five-dose screening at 0.01, 0.1, 1.0, 10, and 100 μM. This assay enabled the determination of $GI_{50}$ (growth inhibitory concentration) and $LC_{50}$ (lethal concentration) values. Compounds were considered active when they achieved a selectivity index $LC_{50}/GI_{50} \geq 100$, ensuring that their antiproliferative effects reflected selective growth inhibition rather than nonspecific cytotoxicity.[48,49] Although **3f**, **3n**, and **3o** frequently exhibited very low $GI_{50}$ values, the separation from their $LC_{50}$ values was often insufficient to meet this threshold. Consequently, part of their apparent activity could not be unequivocally distinguished from nonspecific cytotoxic effects.

In Table 3, results highlighted in blue denote selective antiproliferative activity, whereas those in orange indicate cases where the $LC_{50}/GI_{50}$ ratio fell below the required threshold. Accordingly, the subsequent discussion will focus on the blue results obtained for **3f**, **3n**, and **3o**, particularly those showing activity at concentrations close to 1 μM, in comparison with Osimertinib as the reference drug.

Compound **3f** exhibited the strongest antiproliferative effect against the CAKI-1 renal cancer cell line ($GI_{50}$ = 0.287 μM). It also showed potent activity against NCI-H460 (non-small cell lung cancer, $GI_{50}$ = 1.76 μM), HCT-116 (colon cancer, $GI_{50}$ = 0.699 μM), UACC-257 (melanoma, $GI_{50}$ = 1.05 μM), OVCAR-4 (ovarian cancer, $GI_{50}$ = 1.94 μM), RXF 393 (renal cancer, $GI_{50}$ = 1.13 μM), and MCF7 (breast cancer, $GI_{50}$ = 0.578 μM). Remarkably, compound **3f** displayed higher activity than Osimertinib across all these cell lines (Table 3, bold entries).

For compound **3n**, although it consistently yielded low $GI_{50}$ values across multiple cancer cell lines, it failed to achieve the required 100-fold separation from $LC_{50}$, suggesting that nonspecific cytotoxicity may partly account for its activity profile. Nevertheless, compound **3n** displayed potent and selective antiproliferative activity against hematological malignancies, including CCRF-CEM, K-562, MOLT-4, and RPMI-8226, with $GI_{50}$ values ranging from 0.367 to 1.81 μM. Remarkably, **3n** was 1.3-, 1.1-, and 5.3-fold more potent than Osimertinib against CCRF-CEM, MOLT-4, and RPMI-8226, respectively (Table 3, bold entries). In addition, **3n** showed notable activity against the HCT-116 colon cancer cell line ($GI_{50}$ = 1.76 μM), comparable to Osimertinib ($GI_{50}$ = 1.72 μM).

Compound **3o** exhibited its highest antiproliferative activity against the CAKI-1 renal cancer cell line ($GI_{50}$ = 0.336 μM),

 

Table 3 Antiproliferative activity ($GI_{50}$ and $LC_{50}$) of Knoevenagel adducts **3f**, **3n**, and **3o** against a panel of 60 human cancer cell lines, in comparison with the reference drug Osimertinib (μM)[abcd]

| Panel/Cell line | 3f | | 3n | | 3o | | Osimertinib 779217[d] | |
|---|---|---|---|---|---|---|---|---|
| | $GI_{50}$[a] | $LC_{50}$[b] | $GI_{50}$[a] | $LC_{50}$[b] | $GI_{50}$[a] | $LC_{50}$[b] | $GI_{50}$[a] | $LC_{50}$[b] |
| **Leukemia** | | | | | | | | |
| CCRF-CEM | >100 | >100 | **1.26** | >100 | 40.4 | >100 | 1.61 | 53.4 |
| HL-60(TB) | >100 | >100 | 0.534 | 49.9 | 23.9 | >100 | 1.47 | 7.53 |
| K-562 | 42.5 | >100 | 1.81 | >100 | 5.88 | >100 | 1.72 | 77.6 |
| MOLT-4 | >100 | >100 | **1.65** | >100 | 22.2 | >100 | 1.77 | 48.1 |
| RPMI-8226 | 37.2 | >100 | **0.367** | >100 | 5.93 | >100 | 1.95 | 90.7 |
| SR | >100 | >100 | –[c] | –[c] | –[c] | –[c] | 1.29 | >100 |
| **Non-Small Cell Lung Cancer** | | | | | | | | |
| A549/ATCC | 54.3 | >100 | 1.51 | 10.6 | 6.99 | >100 | 1.40 | 17.3 |
| EKVX | >100 | >100 | 11.4 | 48.7 | 94.1 | >100 | 7.52 | 23.4 |
| HOP-62 | 3.43 | >100 | 1.80 | 46.6 | 5.05 | >100 | 4.07 | 46.3 |
| HOP-92 | 48.8 | >100 | 0.701 | 8.66 | 24.8 | >100 | 7.92 | 38.8 |
| NCI-H226 | 0.196 | 3.43 | 0.254 | 2.97 | 0.139 | 1.72 | 3.93 | 57.9 |
| NCI-H23 | 18.1 | >100 | 1.81 | 9.65 | 5.73 | >100 | 4.75 | 57.1 |
| NCI-H322M | >100 | >100 | 1.49 | 7.85 | >100 | >100 | 1.75 | 27.3 |
| NCI-H460 | **1.76** | >100 | 0.897 | 5.60 | **0.545** | >100 | 2.18 | 17.1 |
| NCI-H522 | >100 | >100 | 1.47 | 6.20 | >100 | >100 | 1.69 | 5.98 |
| **Colon Cancer** | | | | | | | | |
| COLO 205 | 21.3 | >100 | 2.46 | 44.0 | 5.20 | >100 | 1.62 | 6.08 |
| HCC-2998 | >100 | >100 | 1.55 | 5.49 | 30.2 | >100 | 1.56 | 7.26 |
| HCT-116 | **0.699** | >100 | 1.76 | >100 | **0.933** | >100 | 1.72 | 6.32 |
| HCT-15 | >100 | >100 | 1.45 | 7.55 | 37.2 | >100 | 1.61 | 8.49 |
| HT29 | 14.9 | >100 | 1.66 | 7.86 | 6.62 | >100 | 1.84 | 12.7 |
| KM12 | >100 | >100 | 1.09 | 5.34 | >100 | >100 | 2.31 | 16.1 |
| SW-620 | 9.86 | >100 | 1.63 | 6.86 | 3.74 | >100 | 1.83 | 7.71 |
| **CNS Cancer** | | | | | | | | |
| SF-268 | 74.7 | >100 | 1.81 | 14.1 | >100 | >100 | 1.95 | 33.8 |
| SF-295 | 4.35 | >100 | 2.20 | 23.0 | **1.74** | >100 | 2.75 | 29.8 |
| SF-539 | 98.5 | >100 | 1.01 | 4.70 | >100 | >100 | 1.71 | 6.34 |
| SNB-19 | 49.3 | >100 | 1.33 | 5.24 | 53.6 | >100 | 2.69 | 66.5 |
| SNB-75 | 20.4 | >100 | 0.785 | 5.35 | >100 | >100 | 3.52 | 43.4 |
| U251 | 2.10 | >100 | 1.25 | 5.15 | **1.58** | >100 | 1.63 | 6.50 |
| **Melanoma** | | | | | | | | |
| LOX IMVI | >100 | >100 | 1.25 | 5.27 | 49.8 | >100 | 1.75 | 7.19 |
| MALME-3M | 50.2 | >100 | 1.43 | 5.67 | >100 | >100 | 2.16 | 7.16 |
| M14 | >100 | >100 | 1.96 | 16.5 | >100 | >100 | 1.91 | 6.81 |
| MDA-MB-435 | >100 | >100 | 1.58 | 7.22 | 92.1 | >100 | 1.62 | 5.68 |
| SK-MEL-2 | –[c] | –[c] | 1.40 | 6.34 | 6.03 | >100 | 2.08 | 7.85 |
| SK-MEL-28 | >100 | >100 | 1.72 | 6.07 | >100 | >100 | 1.63 | 5.79 |
| SK-MEL-5 | 15.5 | >100 | 1.64 | 6.99 | 1.88 | 56.8 | 1.72 | 5.69 |
| UACC-257 | **1.05** | >100 | 1.35 | 6.28 | 0.275 | 5.21 | 1.71 | 6.28 |
| UACC-62 | 0.328 | 4.77 | 1.26 | 5.70 | 0.193 | 3.27 | 1.85 | 7.05 |
| **Ovarian cancer** | | | | | | | | |
| IGROV1 | 1.28 | 69.0 | 1.38 | 6.13 | **0.390** | >100 | 1.14 | 53.8 |
| OVCAR-3 | 4.77 | >100 | 1.35 | 5.80 | 1.96 | >100 | 1.40 | 6.14 |
| OVCAR-4 | **1.94** | >100 | 2.20 | 27.6 | **1.09** | >100 | 2.74 | 83.2 |
| OVCAR-5 | 1.12 | 9.14 | 1.92 | 10.0 | 0.244 | 5.75 | 1.30 | 6.71 |
| OVCAR-8 | 38.3 | >100 | 1.63 | 8.41 | 60.6 | >100 | 2.04 | 29.4 |
| NCI/ADR-RES | –[c] | –[c] | 1.56 | 7.59 | 39.8 | >100 | 1.84 | 51.4 |
| SK-OV-3 | 21.9 | >100 | 12.6 | 58.5 | 24.5 | >100 | 0.0370 | 47.5 |
| **Renal Cancer** | | | | | | | | |
| 786-0 | 30.5 | >100 | 2.10 | 8.66 | 6.16 | >100 | 1.40 | 6.16 |
| A498 | 1.19 | 7.49 | 1.61 | 5.49 | 1.02 | 5.02 | 1.11 | 10.50 |
| ACHN | 68.6 | >100 | 1.57 | 5.47 | >100 | >100 | 0.272 | 4.88 |
| CAKI-1 | **0.287** | 40.2 | 0.776 | 4.70 | **0.336** | >100 | 0.343 | 30.1 |
| RXF 393 | **1.13** | >100 | 1.44 | 5.44 | 28.7 | >100 | 1.45 | 6.61 |
| SN12C | >100 | >100 | 1.34 | 6.53 | 83.1 | >100 | 2.20 | 32.1 |
| TK-10 | 0.911 | 17.7 | 2.10 | 6.17 | 1.05 | 9.48 | 0.0615 | 45.7 |
| UO-31 | 18.2 | >100 | 1.16 | 4.88 | 14.7 | >100 | 0.604 | 19.5 |
| **Prostate Cancer** | | | | | | | | |
| PC-3 | >100 | >100 | 1.51 | 21.4 | 46.1 | >100 | 2.74 | 39.4 |
| DU-145 | >100 | >100 | 1.14 | 4.88 | >100 | >100 | 1.76 | 36.0 |
| **Breast Cancer** | | | | | | | | |
| MCF7 | **0.578** | >100 | 0.391 | 6.64 | **0.397** | >100 | 1.50 | 8.02 |
| MDA-MB-231/ATCC | >100 | >100 | 1.56 | 6.73 | >100 | >100 | 1.59 | 7.48 |
| HS 578T | 44.1 | >100 | 2.12 | >100 | >100 | >100 | 3.31 | >100 |
| BT-549 | >100 | >100 | 1.74 | 9.85 | >100 | >100 | 3.52 | 40.8 |
| T-47D | 0.862 | 75.7 | 0.279 | 8.50 | **0.345** | >100 | 8.15 | 55.2 |
| MDA-MB-468 | 0.122 | 0.676 | 0.290 | 3.66 | 0.0887 | 0.595 | 2.71 | 4.45 |

[a] $GI_{50}$ corresponds to the concentration required to reduce net protein content by 50% in control cells, as determined by the SRB assay, after exposure to five concentrations (0.01, 0.1, 1.0, 10, and 100 μM). [b] $LC_{50}$ represents the concentration needed to induce 50% cell death. [c] Not determined. [d] Activity data for Osimertinib in the NCI-60 cancer cell line panel were obtained from the NCI database: https://dtp.cancer.gov/dtpstandard/cancerscreeningdata/index.jsp.

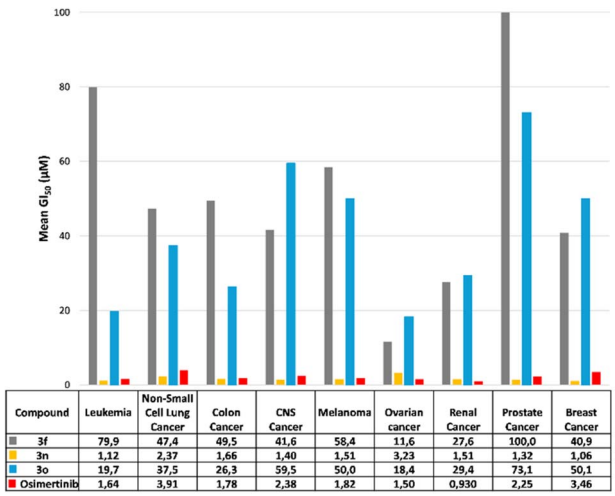


| Compound | Leukemia | Non-Small Cell Lung Cancer | Colon Cancer | CNS Cancer | Melanoma | Ovarian cancer | Renal Cancer | Prostate Cancer | Breast Cancer |
|---|---|---|---|---|---|---|---|---|---|
| 3f | 79,9 | 47,4 | 49,5 | 41,6 | 58,4 | 11,6 | 27,6 | 100,0 | 40,9 |
| 3n | 1,12 | 2,37 | 1,66 | 1,40 | 1,51 | 3,23 | 1,51 | 1,32 | 1,06 |
| 3o | 19,7 | 37,5 | 26,3 | 59,5 | 50,0 | 18,4 | 29,4 | 73,1 | 50,1 |
| Osimertinib | 1,64 | 3,91 | 1,78 | 2,38 | 1,82 | 1,50 | 0,930 | 2,25 | 3,46 |

Fig. 4 Mean $GI_{50}$ values per panel for compounds **3f**, **3n**, and **3o** compared with the reference drug Osimertinib across the NCI-60 human cancer cell line panel.

showing comparable potency to Osimertinib ($GI_{50} = 0.343$ μM). It also demonstrated strong activity against NCI-H460 (non-small cell lung cancer, $GI_{50} = 0.545$ μM), HCT-116 (colon cancer, $GI_{50} = 0.933$ μM), SF-295 (CNS cancer, $GI_{50} = 1.74$ μM), and U251 (CNS cancer, $GI_{50} = 1.58$ μM), surpassing Osimertinib in these cell lines (Table 3, bold entries). Moreover, **3o** displayed notable potency against ovarian cancer cell lines IGROV1, OVCAR-4, and OVCAR-3, with $GI_{50}$ values of 0.390 μM, 1.09 μM, and 1.96 μM, respectively, being 2.9- and 2.5-fold more potent than Osimertinib against IGROV1 and OVCAR-4. Finally, **3o** exerted pronounced antiproliferative effects against the breast cancer cell lines T47D and MCF7, with $GI_{50}$ values of 0.345 μM and 0.397 μM, respectively, corresponding to 23.6- and 3.8-fold greater potency than Osimertinib.

Taken together, compounds **3f** and **3o** incorporating a primary amide (–$CONH_2$) and an ethyl ester (–COOEt), respectively, exhibited potent and selective antiproliferative activity at concentrations close to 1 μM across multiple cancer types, including non-small cell lung (NCI-H460), colon (HCT-116), ovarian (OVCAR-4), renal (CAKI-1), and breast (MCF7), with $GI_{50}$ values ranging from 0.287 μM to 1.94 μM ($LC_{50}/GI_{50} \geq 100$ for all cases). Notably, both compounds exhibited their strongest activity against the CAKI-1 renal cancer cell line, with $GI_{50}$ values of 0.287 μM for **3f** and 0.336 μM for **3o**, closely comparable to Osimertinib ($GI_{50} = 0.343$ μM).

In contrast, compound **3n**, bearing two primary amide groups and lacking the cyano substituent, exhibited both low $GI_{50}$ and $LC_{50}$ values, suggesting that replacement of –CN with –$CONH_2$ may promote nonspecific cytotoxicity ($GI_{50} \approx LC_{50}$). Despite this, **3n** maintained selective antiproliferative activity against hematological cell lines CCRF-CEM, K-562, MOLT-4, and RPMI-8226 ($GI_{50} = 0.367$–$1.81$ μM), where it proved more potent than Osimertinib in most cases ($GI_{50} = 1.61$–$1.95$ μM).

Importantly, compounds **3f**, **3o**, and **3n** also exhibited reproducible antiproliferative activity against the HCT-116 colon cancer cell line, with $GI_{50}$ values of 0.699 μM, 0.933 μM, and 1.76 μM, respectively ($LC_{50}/GI_{50} \geq 100$ for all cases). Notably, compounds **3f** and **3o** were 2.5- and 1.8-fold more potent than Osimertinib, whereas **3n** showed comparable potency to the reference drug.

Overall, these findings underscore that the Knoevenagel adducts **3f**, **3n**, and **3o**, featuring an *N*,*N*-diphenylamino substituent, represent highly promising molecular scaffolds for the rational design and development of new anticancer agents.

Additionally, the mean $GI_{50}$ values for the cancer panels of compounds **3f**, **3n**, and **3o** were compared with those of the reference drug Osimertinib (Fig. 4). Among them, compound **3n** exhibited consistently higher antiproliferative activity than **3f** and **3o** across all cancer types. Remarkably, **3n** was more potent than Osimertinib in leukemia, non-small cell lung, colon, CNS, melanoma, prostate, and breast cancer panels, with fold increases of 1.5, 1.6, 1.1, 1.7, 1.2, 1.7, and 3.3, respectively.

Table 4 Toxicological properties of compounds **3f**, **3n**, and **3o**.[a,b]

| Property | 3f | 3n | 3o |
|---|---|---|---|
| Mean $LC_{50}$ (μM) | 89.68 | 23.09 | 89.98 |
| NR-AhR | 0.062 | 0.0 | **0.489** |
| NR-AR | 0.001 | 0.0 | 0.003 |
| NR-AR-LBD | 0.165 | **0.537** | 0.056 |
| NR-Aromatase | 0.029 | 0.0 | 0.214 |
| NR-ER | **0.379** | 0.036 | **0.395** |
| NR-ER-LBD | 0.074 | 0.002 | 0.132 |
| NR-PPAR-gamma | 0.007 | 0.0 | 0.002 |
| SR-ARE | **0.839** | **0.762** | **0.789** |
| SR-ATAD5 | 0.005 | 0.0 | 0.003 |
| SR-HSE | 0.021 | 0.029 | 0.028 |
| SR-MMP | **0.670** | 0.101 | **0.568** |
| SR-p53 | **0.317** | **0.489** | 0.205 |

[a] Data obtained from https://admetlab3.scbdd.com/server/evaluation. [b] Risk classification: excellent/low (green, <0.3), moderate (yellow, 0.3–0.7), and poor/high (red, >0.7).

These findings suggest that **3n** may serve as a promising lead molecule for anticancer drug discovery; however, its activity cannot be clearly differentiated from nonspecific cytotoxic effects ($GI_{50} \approx LC_{50}$), a limitation also observed for Osimertinib across multiple cancer cell lines (Table 3).

### 2.6 Mechanistic toxicological profiling

To complement the experimental cytotoxicity data ($LC_{50}$ values, Table 3) and to elucidate potential molecular mechanisms underlying the observed nonspecific cytotoxicity, a Tox21 pathway analysis was performed using ADMETlab 3.0. This computational tool predicts the likelihood of activation or inhibition of nuclear receptor (NR) and stress response (SR) pathways, with output values ranging from 0 (inactive) to 1 (active). According to ADMETlab's classification, predictions are categorized as excellent/low risk (green, <0.3), moderate (yellow, 0.3–0.7), and poor/high risk (red, >0.7). The analyzed endpoints included NR-AhR (oxidative stress and xenobiotic metabolism), NR-AR and NR-AR-LBD (androgen receptor and its ligand-binding domain; endocrine signaling), NR-Aromatase (estrogen biosynthesis and endocrine disruption), NR-ER and NR-ER-LBD (estrogen receptor and its ligand-binding domain; hormonal regulation), NR-PPAR-gamma (lipid metabolism and inflammatory response), SR-ARE (Nrf2-mediated oxidative stress response), SR-ATAD5 (genomic integrity maintenance), SR-HSE (cellular stress induced by protein misfolding), SR-MMP (mitochondrial dysfunction and apoptosis), and SR-p53 (DNA damage response and apoptosis). As shown in Table 4, compounds **3f**, **3n**, and **3o** exhibited mean $LC_{50}$ values of 89.68, 23.09, and 89.98 μM, respectively. All compounds exhibited moderate probabilities of activation for the Nrf2-mediated oxidative stress pathway (SR-ARE = 0.762–0.839), suggesting potential induction of adaptive antioxidant mechanisms. Notably, compound **3n** displayed additional moderate activity toward androgen receptor binding (NR-AR-LBD = 0.537) and p53-dependent DNA damage response (SR-p53 = 0.489), which may be associated with its higher cytotoxic effect. These results indicate that the nonspecific cytotoxicity of **3n** likely arises from the combined influence of oxidative stress, hormonal signaling, and apoptotic mechanisms. Enhanced Nrf2 (SR-ARE) activity may be associated with increased levels of reactive oxygen species, while interaction with the androgen receptor (NR-AR-LBD) could disrupt redox homeostasis and promote oxidative damage that activates the p53-mediated apoptotic pathway.[50,51]

### 2.7 Molecular docking studies

EGFR was selected as the molecular target for docking studies due to its well-established role as a driver in cancer progression and its validation as the clinical target of FDA-approved acrylamide-based inhibitors, such as Osimertinib. The incorporation of the acrylamide moiety not only enables irreversible binding to the EGFR kinase domain but has also been shown to enhance drug-like properties in EGFR inhibitor design.[42,52] Given that compounds **3f**, **3n**, and **3o** demonstrated notable antiproliferative activity comparable or superior to Osimertinib across multiple NCI-60 cancer cell lines, targeting EGFR *via* docking provided a rational framework to correlate their biological activity with their predicted binding conformations.[53]

Molecular docking studies were conducted to evaluate the interactions of the Knoevenagel adducts **3f**, **3n**, and **3o** with the EGFR active site (PDB ID: 1M17). To ensure accuracy and energetic plausibility of the predicted binding poses, the docking protocol was validated by redocking the co-crystallized ligands into its binding site. This validation confirmed that AutoDock Vina reliably reproduced the experimental orientation and position of the ligand,[54] with redocking yielded RMSD values below 2.0 Å, thereby verifying the robustness of the docking parameters. Self-docking of the co-crystallized ligand Erlotinib resulted in a docking score of −6.6 kcal $mol^{-1}$ and an RMSD of 1.31 Å, validating the protocol. These results confirmed the reliability and accuracy of the molecular docking simulations applied in this study.

To further investigate the binding interactions of (*E*)-2-cyano-3-arylacrylamide **3f** within the EGFR active site, molecular docking simulations revealed that its acrylamide moiety occupied the region typically filled by the quinazoline ring of Erlotinib, forming two key hydrogen bonds with Met769 and an additional hydrogen bond with Pro770 (Fig. 5 and 6). The *para*-disubstituted benzene ring of **3f** was oriented toward the hydrophobic side chains of Val702 and Leu820. In this conformation, one benzene ring overlapped with the region commonly occupied by the anilino moiety of Erlotinib, while the second benzene ring extended toward the opposite side of the binding pocket, engaging in several non-covalent interactions, including a π–alkyl interaction with Val702, a π–cation interaction with Lys721, and π–anion and π–σ interactions with Asp831 and Phe699, respectively. Additional van der Waals contacts further stabilized the complex. Overall, compound **3f** engaged six key side-chain residues critical for EGFR inhibition (Leu694, Leu820, Ala719, Met769, Lys721, and Val702), along with three additional active-site residues (Phe699, Pro770, and Asp831) that are not commonly targeted by reference ligands. The remarkable binding affinity of compound **3f** (−8.7 kcal $mol^{-1}$), surpassing that of Erlotinib (−6.6 kcal $mol^{-1}$), highlights its strong interaction with the

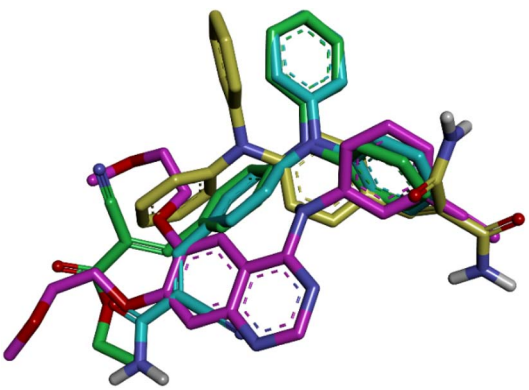

Fig. 5 Overlay of the docked conformations of erlotinib (magenta), compound **3f** (blue), compound **3n** (yellow) and compound **3o** (green) within the EGFR binding pocket.

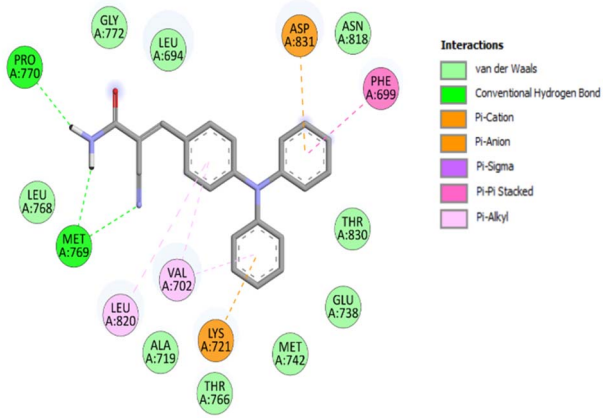


Fig. 6 2D representation of the binding interactions of compound **3f** with key amino acid residues in the EGFR active site.

EGFR binding site and supports its potential as an effective inhibitor.

Following the same docking protocol, compound **3n** was found to occupy the EGFR active site in a binding mode distinct from that of compound **3f**. The acrylamide moiety of **3n** was positioned within the region typically occupied by the anilino moiety of Erlotinib, while one of its benzene rings aligned with the area corresponding to the 2-methoxyethoxy substituent of Erlotinib (Fig. 5). Binding **3n** to the EGFR pocket involved conventional hydrogen bonds with Ala719, Glu738, and Thr830; π–alkyl interactions with Leu694, Val702, and Lys721; along with a π–anion interaction with Asp831. Importantly, compound **3n** preserved five key interactions observed in the reference ligand, involving residues Leu694, Val702, Ala719, Lys721, and Leu820, which are essential for defining the EGFR binding site and its catalytic mechanism. In addition, compound **3n** established novel hydrogen bonds with Glu738 and Thr830, further stabilizing its binding conformation (Fig. 7). The favorable binding affinity of compound **3n** ($-7.8$ kcal mol$^{-1}$), surpassing that of Erlotinib ($-6.6$ kcal mol$^{-1}$), underscores its effective engagement with

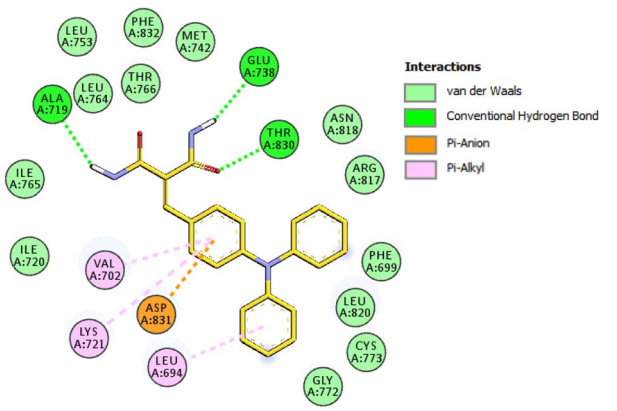


Fig. 7 2D representation of the binding interactions of compound **3n** with key amino acid residues in the EGFR active site.

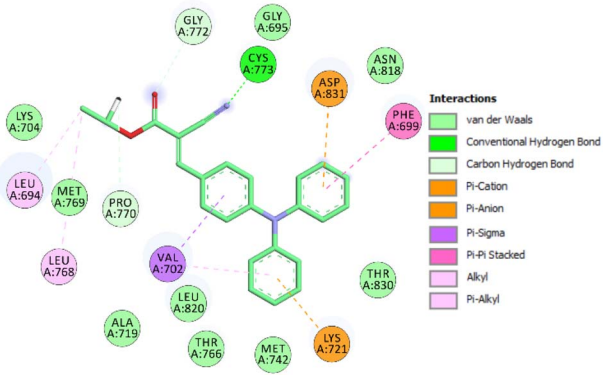


Fig. 8 2D representation of the binding interactions between compound **3o** and key amino acid residues within the EGFR active site.

critical residues in the EGFR active site and supports its potential as a promising inhibitor.

Compound **3o**, with a binding energy of $-7.9$ kcal mol$^{-1}$, displayed interaction patterns with key amino acid residues in the EGFR active site closely resembling those of compound **3f**. Remarkably, the three aromatic rings of compound **3f** overlap with those of **3o**, engaging the same residues (Phe699, Val702, Ala719, Lys721, Met742, Thr766, Asn818, Leu820, Asp831, and Met769) (Fig. 5 and 8). The acrylamide moiety of compound **3o**, although adopting slightly different orientation, forms interactions with several of the same residues (Leu768, Met769, Pro770, and Gly772). The most distinctive feature between the two compounds, and one of mechanistic significance, is the additional interaction with Cys773, a residue that plays a pivotal role in ligand recognition, binding affinity, and selectivity within the EGFR catalytic domain.

## 3 Conclusions

In summary, we developed a piperidine-catalyzed synthesis of (*E*)-2-cyano-3-(het)arylacrylamides **3a–i** in 40–95% yields *via* a Knoevenagel condensation between (hetero)aromatic aldehydes **1a–i** and 2-cyanoacetamide **2a** under mild conditions. The methodology was successfully extended to other methylene active compounds, such as malonamide **2b** and ethyl cyanoacetate **2c**, affording Knoevenagel adducts **3m–o** in 54–81% yields. This strategy is distinguished by its operational simplicity, use of green solvents (water or ethanol), low reaction temperatures, minimal catalyst loading, broad synthetic scope, and straightforward purification by simple filtration in most cases. Additionally, functionalization of the propargyl moiety in α-cyanoacrylamide **5** *via* a CuAAC reaction enabled the synthesis of the 1,4-disubstituted 1,2,3-triazole **6** in 79% yield.

X-ray diffraction analysis of compound **3i** reveals a planar molecular conformation, with the highest electronegative and electropositive potentials (from ESP maps) localized on the carbonyl/cyano and hydroxyl/amino groups, respectively. This distribution of electrostatic potentials, combined with the molecular planarity, accounts for the formation of molecular sheets interconnected through π–π stacking interactions and van der Waals forces.

The antiproliferative activity of Knoevenagel adducts **3a–o** was assessed against the NCI panel of 60 human cancer cell lines using the SRB assay. In the single-dose screening at 10 μM, compounds **3f**, **3n**, and **3o**, each bearing an *N*,*N*-diphenylamino substituent, exhibited the strongest activity within the series, with mean %G values of 40.97, −63.43, and 36.80, respectively.

In the subsequent five-dose screening at 100, 10, 1.0, 0.1, and 0.01 μM, compounds **3f** (bearing a primary amide, –$CONH_2$) and **3o** (bearing an ethyl ester, –COOEt) demonstrated potent and selective antiproliferative activity, with $GI_{50}$ values ranging from 0.287 μM to 1.94 μM and $LC_{50}/GI_{50} \geq 100$ across multiple cancer types, including non-small cell lung (NCI-H460), colon (HCT-116), ovarian (OVCAR-4), renal (CAKI-1), and breast (MCF7). Remarkably, both compounds displayed their strongest activity against the CAKI-1 renal cancer, with $GI_{50}$ values of 0.287 μM for **3f** and 0.336 μM for **3o**, closely comparable to Osimertinib ($GI_{50}$ = 0.343 μM). In contrast, compound **3n** characterized by the presence of two –$CONH_2$ groups and the absence of the cyano substituent, exhibited a cytotoxic profile consistent with nonspecific activity ($GI_{50} \approx LC_{50}$). Despite this limitation, **3n** retained notable selective antiproliferative activity against hematological cancer cell lines CCRF-CEM, K-562, MOLT-4, and RPMI-8226 ($GI_{50}$ = 0.367–1.81 μM), demonstrating superior potency to Osimertinib in most cases ($GI_{50}$ = 1.61–1.95 μM).

Overall, compounds **3f**, **3o**, and **3n** consistently demonstrated antiproliferative activity against the HCT-116 colon cancer cell line, with $GI_{50}$ values of 0.699 μM, 0.933 μM, and 1.76 μM, respectively ($LC_{50}/GI_{50} \geq 100$ in all three cases). Notably, **3f** and **3o** were 2.5- and 1.8-fold more potent than Osimertinib, while **3n** exhibited efficacy comparable to the reference drug. Importantly, molecular docking studies elucidated the binding modes of compounds **3f**, **3n**, and **3o** within the tyrosine kinase domain of the epidermal growth factor receptor (EGFR). These results suggest that the concurrent incorporation of an *N*,*N*-diphenylamino group into *α*,*β*-unsaturated carbonyl scaffolds could provide a privileged structural framework for the rational design and future development of novel anticancer agents.

# 4 Experimental

## 4.1 Materials and methods

The progress of all reactions was monitored by thin-layer chromatography (TLC) using Merck Kieselgel 60 F254 precoated silica gel plates, with visualization under UV light at 254 and 365 nm. Unless otherwise stated, solvents and reagents were purchased from Sigma-Aldrich and used without further purification. Infrared spectra were recorded at room temperature using a PerkinElmer Polymer ID Analyzer equipped with an ATR accessory, operating over a wavenumber range of 400–4000 $cm^{-1}$, with a spectral resolution of 4 $cm^{-1}$ and an acquisition of 64 scans per sample. $^1H$ and $^{13}C$ NMR spectra were obtained using a Bruker Avance 400 MHz spectrometer with DMSO-$d_6$ as the deuterated solvent. Chemical shifts ($\delta$) are reported in parts per million (ppm) relative to residual solvent signals ($\delta$ = 2.50 ppm for $^1H$ and 39.52 ppm for $^{13}C$) and coupling constants ($J$) are expressed in hertz (Hz). Multiplicity is denoted as s (singlet), d (doublet), t (triplet), and m (multiplet). High-resolution mass spectrometry (HRMS) was performed using a Q-TOF 6520 spectrometer with electrospray ionization (ESI, 4000 V).

## 4.2 Knoevenagel synthesis of (*E*)-2-cyano-3-(het) arylacrylamides 3

A mixture of the (hetero)aromatic aldehyde **1a–l** (1 mmol), active methylene compound **2a–c** (1 mmol), and piperidine (0.1 mol, 9.9 μL) in distilled water or absolute ethanol (3 mL) was stirred at room temperature for 6–24 h. The resulting precipitate was filtered, washed with a cold EtOH/$H_2O$ mixture (1 : 1, v/v), and dried to afford the (*E*)-2-cyano-3-(het)arylacrylamides **3a–o**. Crystals of compounds **3i** and **3n** suitable for single-crystal X-ray diffraction analysis were obtained by slow evaporation of a solution of the compound in a mixture of *N*,*N*-dimethylformamide and methanol (1 : 1 v/v, 2 mL) over the course of one month under ambient temperature and pressure conditions. The identity of the products was confirmed by comparison of their NMR data with values reported in the literature.

**4.2.1 (*E*)-3-(4-Chlorophenyl)-2-cyanoacrylamide 3a.** A mixture of 4-chlorobenzaldehyde **1a** (141 mg, 1 mmol), 2-cyanoacetamide **2a** (84 mg, 1 mmol), and piperidine (10 mol%, 10 μL) was stirred at room temperature for 6 h to afford compound **3a** as a white solid (192 mg, 93%). M.p. 238–239 °C (amorphous) (Lit. 238–240 °C).[55] FTIR (KBr): 3455 ($\nu_{as}$ $NH_2$ non-hydrogen bonded), 3302 ($\nu_s$ $NH_2$ non-hydrogen bonded), 3241 ($\nu_{as}$ $NH_2$ hydrogen bonded), 3154 ($\nu_s$ $NH_2$ hydrogen bonded), 3061, 2211 ($\nu$C≡N), 1704 ($\nu$C=O), 1602 ($\nu$C=C), 1587 ($\nu$C=C), 1486, 1381, 1207, 1092, 1008, 957, 826, 784, 707 ($\nu$C–Cl), 577, 458 $cm^{-1}$. $^1H$ NMR (400 MHz, DMSO-$d_6$): 7.65 (d, $J$ = 8.8 Hz, 2H), 7.82 (br s, 1H, $NH_a$), 7.90–7.97 (m, 3H), 8.18 (s, 1H, H-3) ppm. $^{13}C\{^1H\}$ NMR (101 MHz, DMSO-$d_6$): 107.3 (C), 116.3 (C), 129.4 (2CH), 130.8 (C), 131.7 (2CH), 136.9 (C), 149.3 (CH, C-3), 162.5 (C, CE001O) ppm. These NMR data matched previously reported data.[55]

**4.2.2 (*E*)-3-(4-Bromophenyl)-2-cyanoacrylamide 3b.** A mixture of 4-bromobenzaldehyde **1b** (185 mg, 1 mmol), 2-cyanoacetamide **2a** (84 mg, 1 mmol), and piperidine (10 mol%, 10 μL) was stirred at room temperature for 6 h to afford compound **3b** as a white solid (217 mg, 87%). M.p. 220–221 °C (amorphous) (Lit. 198 °C).[56] FTIR (KBr): 3440 ($\nu_{as}$ $NH_2$ non-hydrogen bonded), 3325 ($\nu_s$ $NH_2$ non-hydrogen bonded), 3256 ($\nu_{as}$ $NH_2$ hydrogen bonded), 3152 ($\nu_s$ $NH_2$ hydrogen bonded), 3053, 2216 ($\nu$C≡N), 1701 ($\nu$C=O), 1602 ($\nu$C=C), 1489, 1378, 1187, 1074, 1008, 829, 811, 697, 580 ($\nu$C–Br), 470 $cm^{-1}$. $^1H$ NMR (400 MHz, DMSO-$d_6$): 7.78 (d, $J$ = 8.4 Hz, 2H), 7.82 (br s, 1H, $NH_a$), 7.86 (d, $J$ = 8.4 Hz, 2H), 7.95 (br s, 1H, $NH_b$), 8.16 (s, 1H, H-3) ppm. $^{13}C\{^1H\}$ NMR (101 MHz, DMSO-$d_6$): 107.4 (C), 116.3 (C), 126.0 (C), 131.2 (C), 131.8 (2CH), 132.4 (2CH), 149.4 (CH, C-3), 162.5 (C, C=O) ppm. These NMR data matched previously reported data.[56]

**4.2.3 (*E*)-2-Cyano-3-(4-nitrophenyl)acrylamide 3c.** A mixture of 4-nitrobenzaldehyde **1c** (151 mg, 1 mmol), 2-cyanoacetamide **2a** (84 mg, 1 mmol), and piperidine (10 mol%, 10 μL) was stirred at room temperature for 24 h to afford

compound **3c** as a brown solid (145 mg, 67%). M.p. 200–201 °C (amorphous) (Lit. 198–200 °C).[56] FTIR (ATR): 3438 ($\nu_{as}$ $NH_2$ non-hydrogen bonded), 3344 ($\nu_s$ $NH_2$ non-hydrogen bonded), 3287 ($\nu_{as}$ $NH_2$ hydrogen bonded), 3193 ($\nu_s$ $NH_2$ hydrogen bonded), 3049, 2224 ($\nu$C≡N), 1690 ($\nu$C=O), 1602 ($\nu$C=C), 1509, 1380, 1344, 1203, 1106, 855, 782, 769, 748, 683, 568, 531, 474, 443 $cm^{-1}$. $^1H$ NMR (400 MHz, DMSO-$d_6$): 7.93 (br s, 1H, $NH_a$), 8.06 (br s, 1H, $NH_b$), 8.12 (d, $J$ = 8.8 Hz, 2H), 8.30 (s, 1H, H-3), 8.37 (d, $J$ = 8.4 Hz, 2H) ppm. $^{13}C\{^1H\}$ NMR (101 MHz, DMSO-$d_6$): 110.6 (C), 115.8 (C), 124.2 (2CH), 131.0 (2CH), 138.1 (C), 148.3 (CH, C-3), 148.8 (C), 162.1 (C, C=O) ppm. These NMR data matched previously reported data.[56]

**4.2.4 (*E*)-2-Cyano-3-(2,4-dichlorophenyl)acrylamide 3d.** A mixture of 2,4-dichlorobenzaldehyde **1d** (175 mg, 1 mmol), 2-cyanoacetamide **2a** (84 mg, 1 mmol), and piperidine (10 mol%, 10 μL) was stirred at room temperature for 6 h to afford compound **3d** as a white solid (192 mg, 80%). M.p. 178–179 °C (amorphous) (Lit. 125 °C).[56] FTIR (KBr): 3399 ($\nu_{as}$ $NH_2$ non-hydrogen bonded), 3347 ($\nu_s$ $NH_2$ non-hydrogen bonded), 3255 ($\nu_{as}$ $NH_2$ hydrogen bonded), 3182 ($\nu_s$ $NH_2$ hydrogen bonded), 3090, 2230 ($\nu$C≡N), 1715 ($\nu$C=O), 1608 ($\nu$C=C), 1585 ($\nu$C=C), 1470, 1393, 1144, 1110, 1051, 924, 842, 826, 792, 765, 592, 559, 532, 446 $cm^{-1}$. $^1H$ NMR (400 MHz, DMSO-$d_6$): 7.65 (dd, $J$ = 2.0, 8.8 Hz, 1H), 7.86 (d, $J$ = 2.0 Hz, 1H), 7.94 (br s, 1H, $NH_a$), 8.01 (d, $J$ = 8.4 Hz, 1H), 8.08 (br s, 1H, $NH_b$), 8.30 (s, 1H, H-3) ppm. $^{13}C\{^1H\}$ NMR (101 MHz, DMSO-$d_6$): 111.5 (C), 115.4 (C), 128.2 (CH), 129.5 (C), 129.7 (CH), 130.9 (CH), 135.1 (C), 137.0 (C), 146.0 (CH, C-3), 161.6 (C, C=O) ppm. These NMR data matched previously reported data.[56]

**4.2.5 (*E*)-3-(4-Chloro-3-nitrophenyl)-2-cyanoacrylamide 3e.** A mixture of 4-chloro-3-nitrobenzaldehyde **1e** (185 mg, 1 mmol), 2-cyanoacetamide **2a** (84 mg, 1 mmol), and piperidine (10 mol%, 10 μL) was stirred at room temperature for 6 h to afford compound **3e** as a brown solid (218 mg, 87%). M.p. 164–165 °C (amorphous). FTIR (ATR): 3404 ($\nu_{as}$ $NH_2$ non-hydrogen bonded), 3324 ($\nu_s$ $NH_2$ non-hydrogen bonded), 3249 ($\nu_{as}$ $NH_2$ hydrogen bonded), 3179 ($\nu_s$ $NH_2$ hydrogen bonded), 3076, 2223 ($\nu$C≡N), 1707 ($\nu$C=O), 1607 ($\nu$C=C), 1538, 1478, 1392, 1352, 1213, 1112, 1052, 941, 824, 789, 670, 581, 524, 488, 451 $cm^{-1}$. $^1H$ NMR (400 MHz, DMSO-$d_6$): 7.92 (br s, 1H, $NH_a$), 8.00 (d, $J$ = 8.4 Hz, 1H), 8.01 (br s, 1H, $NH_b$), 8.21 (dd, $J$ = 2.2, 8.6 Hz, 1H), 8.25 (s, 1H, H-3), 8.56 (d, $J$ = 2.0 Hz, 1H) ppm. $^{13}C\{^1H\}$ NMR (101 MHz, DMSO-$d_6$): 109.9 (C), 115.7 (C), 127.0 (CH), 128.2 (C), 132.3 (C), 132.7 (CH), 134.2 (CH), 147.3 (CH, C-3), 147.6 (C), 161.9 (C, C=O) ppm. HRMS (ESI+): $m/z$ calculated for $C_{10}H_7{}^{35}ClN_3O_3^+$ 252.0170 $[M + H]^+$; found 252.0176.

**4.2.6 (*E*)-2-Cyano-3-(4-(diphenylamino)phenyl)acrylamide 3f.** A mixture of 4-(diphenylamino)benzaldehyde **1f** (273 mg, 1 mmol), 2-cyanoacetamide **2a** (84 mg, 1 mmol), and piperidine (10 mol%, 10 μL) was stirred at room temperature for 24 h to afford compound **3f** as a yellow solid (299 mg, 88%). M.p. 263–265 °C (amorphous) (Lit. 263–265 °C).[43] FTIR (ATR): 3403 ($\nu_{as}$ $NH_2$ non-hydrogen bonded), 3325 ($\nu_s$ $NH_2$ non-hydrogen bonded), 3288 ($\nu_{as}$ $NH_2$ hydrogen bonded), 3177 ($\nu_s$ $NH_2$ hydrogen bonded), 3065, 2220 ($\nu$C≡N), 1652 ($\nu$C=O), 1607 ($\nu$C=C), 1576 ($\nu$C=C), 1490, 1368, 1326, 1301, 1193, 1179, 1075, 926, 834, 826, 756, 7256.89 (d, $J$ = 8.8 Hz, 2H), 7.16–7.25 (m, 6H), 7.41 (dd, $J$ = 7.6, 7.6 Hz, 4H), 7.62 (br s, 1H, $NH_a$), 7.75 (br s, 1H, $NH_b$), 7.82 (d, $J$ = 8.8 Hz, 2H), 8.02 (s, 1H, H-3) ppm. $^{13}C\{^1H\}$ NMR (101 MHz, DMSO-$d_6$): 101.4 (C), 117.4 (C), 118.7 (2CH), 123.5 (C), 125.4 (2CH), 126.2 (4CH), 130.0 (4CH), 132.1 (2CH), 145.5 (2C), 149.8 (CH, C-3), 151.1 (C), 163.3 (C, C=O) ppm. These NMR data matched previously reported data.[43]

**4.2.7 (*E*)-2-Cyano-3-(*p*-tolyl)acrylamide 3g.** A mixture of 4-methylbenzaldehyde **1g** (118 μL, 1 mmol), 2-cyanoacetamide **2a** (84 mg, 1 mmol), and piperidine (10 mol%, 10 μL) was stirred at room temperature for 6 h to afford compound **3g** as a white solid (130 mg, 70%). M.p. 162–163 °C (amorphous) (Lit. 205–206 °C).[55] FTIR (ATR): 3382 ($\nu_{as}$ $NH_2$ non-hydrogen bonded), 3339 ($\nu_s$ $NH_2$ non-hydrogen bonded), 3250 ($\nu_{as}$ $NH_2$ hydrogen bonded), 3151 ($\nu_s$ $NH_2$ hydrogen bonded), 3037, 2218 ($\nu$C≡N), 1692 ($\nu$C=O), 1589 ($\nu$C=C), 1508, 1366, 1212, 1182, 1104, 822, 790, 670, 600, 511, 488, 458 $cm^{-1}$. $^1H$ NMR (400 MHz, DMSO-$d_6$): 2.38 (s, 3H), 7.38 (d, $J$ = 8.0 Hz, 2H), 7.74 (br s, 1H, $NH_a$), 7.85 (d, $J$ = 8.0 Hz, 2H), 7.89 (br s, 1H, $NH_b$), 8.13 (s, 1H, H-3) ppm. $^{13}C\{^1H\}$ NMR (101 MHz, DMSO-$d_6$): 21.3 ($CH_3$), 105.3 (C), 116.7 (C), 129.2 (C), 129.9 (2CH), 130.2 (2CH), 143.0 (C), 150.5 (CH, C-3), 162.9 (C, C=O) ppm. These NMR data matched previously reported data.[55]

**4.2.8 (*E*)-2-Cyano-3-(4-methoxyphenyl)acrylamide 3h.** A mixture of 4-methoxybenzaldehyde **1h** (121 μL, 1 mmol), 2-cyanoacetamide **2a** (84 mg, 1 mmol), and piperidine (10 mol%, 10 μL) was stirred at room temperature for 6 h to afford compound **3h** as a white solid (160 mg, 79%). M.p. 210–211 °C (amorphous) (Lit. 207–209 °C).[56] FTIR (ATR): 3445 ($\nu_{as}$ $NH_2$ non-hydrogen bonded), 3304 ($\nu_s$ $NH_2$ non-hydrogen bonded), 3231 ($\nu_{as}$ $NH_2$ hydrogen bonded), 3164 ($\nu_s$ $NH_2$ hydrogen bonded), 3067, 2208 ($\nu$C≡N), 1694 ($\nu$C=O), 1581 ($\nu$C=C), 1384, 1364, 1310, 1260, 1177, 1025, 961, 825, 672, 578, 550, 530, 472, 455 $cm^{-1}$. $^1H$ NMR (400 MHz, DMSO-$d_6$): 3.85 (s, 3H), 7.13 (d, $J$ = 8.8 Hz, 2H), 7.68 (br s, 1H, $NH_a$), 7.81 (br s, 1H, $NH_b$), 7.96 (d, $J$ = 8.8 Hz, 2H), 8.11 (s, 1H, H-3) ppm. $^{13}C\{^1H\}$ NMR (101 MHz, DMSO-$d_6$): 55.6 ($CH_3$), 102.9 (C), 114.8 (2CH), 117.1 (C), 124.4 (C), 132.5 (2CH), 150.2 (CH, C-3), 162.6 (C), 163.1 (C, C=O) ppm. These NMR data matched previously reported data.[56]

**4.2.9 (*E*)-2-Cyano-3-(4-hydroxyphenyl)acrylamide 3i.** A mixture of 4-hydroxybenzaldehyde **1i** (122 mg, 1 mmol), 2-cyanoacetamide **2a** (84 mg, 1 mmol), and piperidine (10 mol%, 10 μL) was stirred at room temperature for 12 h to afford compound **3i** as a yellow solid (137 mg, 73%). M.p. 256–258 °C (amorphous) (Lit. 242–243 °C).[56] FTIR (ATR): 3546 ($\nu$O–H), 3450 ($\nu_{as}$ $NH_2$ non-hydrogen bonded), 3363 ($\nu_s$ $NH_2$ non-hydrogen bonded), 3243 ($\nu_{as}$ $NH_2$ hydrogen bonded), 3178 ($\nu_s$ $NH_2$ hydrogen bonded), 3041, 2228 ($\nu$C≡N), 1652 ($\nu$C=O), 1599 ($\nu$C=C), 1570 ($\nu$C=C), 1511, 1411, 1374, 1288, 1229, 1180, 956, 930, 671, 568, 543, 525, 503, 488, 431 $cm^{-1}$. $^1H$ NMR (400 MHz, DMSO-$d_6$): 6.93 (d, $J$ = 8.8 Hz, 2H), 7.63 (br s, 1H, $NH_a$), 7.76 (br s, 1H, $NH_b$), 7.87 (d, $J$ = 8.8 Hz, 2H), 8.05 (s, 1H, H-3), 10.59 (br s, 1H, OH) ppm. $^{13}C\{^1H\}$ NMR (101 MHz, DMSO-$d_6$): 101.5 (C), 116.2 (2CH), 117.4 (C), 123.0 (C), 132.9 (2CH), 150.5 (CH, C-3), 161.8 (C), 163.4 (C, C=O) ppm. These NMR data matched previously reported data.[56]

**4.2.10 (*E*)-2-Cyano-3-(4-(dimethylamino)phenyl)acrylamide 3j.** A mixture of 4-(dimethylamino)benzaldehyde **1j** (149 mg, 1

 

mmol), 2-cyanoacetamide **2a** (84 mg, 1 mmol), and piperidine (10 mol%, 10 μL) was stirred at room temperature for 6 h to afford compound **3j** as an orange solid (116 mg, 54%). M.p. 192–193 °C (amorphous) (Lit. 213–214 °C).[57] FTIR (ATR): 3405 ($\nu_{as}$ $NH_2$ non-hydrogen bonded), 3373 ($\nu_s$ $NH_2$ non-hydrogen bonded), 3270 ($\nu_{as}$ $NH_2$ hydrogen bonded), 3155 ($\nu_s$ $NH_2$ hydrogen bonded), 3090, 2200 ($\nu$C≡N), 1686 ($\nu$C=O), 1610 ($\nu$C=C), 1562 ($\nu$C=C), 1522, 1440, 1362, 1323, 1238, 1190, 1169, 943, 810, 663, 590, 525, 501, 461 $cm^{-1}$. $^1H$ NMR (400 MHz, DMSO-$d_6$): 3.04 (s, 6H), 6.81 (d, $J$ = 8.8 Hz, 2H), 7.48 (br s, 1H, $NH_a$), 7.58 (br s, 1H, $NH_b$), 7.85 (d, $J$ = 8.8 Hz, 2H), 7.97 (s, 1H, H-3) ppm. $^{13}C\{^1H\}$ NMR (101 MHz, DMSO-$d_6$): 39.6 ($CH_3$), 97.2 (C), 111.6 (2CH), 118.3 (C), 118.7 (C), 132.7 (2CH), 150.5 (CH, C-3), 153.0 (C), 164.0 (C, C=O) ppm. These NMR data matched previously reported data.[57]

**4.2.11 (*E*)-3-(Anthracen-9-yl)-2-cyanoacrylamide 3k.** A mixture of anthracene-9-carbaldehyde **1k** (206 mg, 1 mmol), 2-cyanoacetamide **2a** (84 mg, 1 mmol), and piperidine (10 mol%, 10 μL) was stirred at room temperature for 24 h to afford compound **3k** as a yellow solid (231 mg, 85%). M.p. 280–282 °C (amorphous) (Lit. 280–282 °C).[43] $^1H$ NMR (400 MHz, DMSO-$d_6$): 7.58–7.67 (m, 4H), 8.00–8.04 (m, 3H), 8.19 (d, $J$ = 7.6 Hz, 2H), 8.37 (br s, 1H, $NH_b$), 8.78 (s, 1H), 9.07 (s, 1H, H-3) ppm. $^{13}C\{^1H\}$ NMR (101 MHz, DMSO-$d_6$): 115.1 (C), 117.6 (C), 124.9 (2CH), 125.8 (2CH), 126.4 (C), 127.1 (2CH), 128.2 (2C), 129.0 (2CH), 129.3 (CH), 130.6 (2C), 150.0 (CH, C-3), 162.1 (C, C=O) ppm. These NMR data matched previously reported data.[43]

**4.2.12 (*E*)-2-Cyano-3-(5-(hydroxymethyl)furan-2-yl) acrylamide 3l.** A mixture of 5-(hydroxymethyl)furfural **1l** (126 mg, 1 mmol), 2-cyanoacetamide **2a** (84 mg, 1 mmol), and piperidine (10 mol%, 10 μL) was stirred at room temperature for 12 h to afford compound **3l** as a yellow solid (77 mg, 40%). M.p. 155–156 °C (amorphous) (Lit. 155–156 °C).[40] FTIR (ATR): 3393 ($\nu_{as}$ $NH_2$ non-hydrogen bonded), 3322 ($\nu_s$ $NH_2$ non-hydrogen bonded), 3269 ($\nu_{as}$ $NH_2$ hydrogen bonded), 3204 ($\nu$O–H), 3178 ($\nu_s$ $NH_2$ hydrogen bonded), 3046, 2214 ($\nu$C≡N), 1686 ($\nu$C=O), 1594 ($\nu$C=C), 1569 ($\nu$C=C), 1512, 1390, 1356, 1204, 1024, 973, 939, 799, 741, 631, 615, 536, 453 $cm^{-1}$. $^1H$ NMR (400 MHz, DMSO-$d_6$): 4.50 (d, $J$ = 6.0 Hz, 2H), 5.55 (t, $J$ = 6.0 Hz, 1H, OH), 6.64 (d, $J$ = 4.4 Hz, 1H), 7.33 (d, $J$ = 4.4 Hz, 1H), 7.68 (br s, 1H, $NH_a$), 7.79 (br s, 1H, $NH_b$), 7.93 (s, 1H, H-3) ppm. $^{13}C\{^1H\}$ NMR (101 MHz, DMSO-$d_6$): 56.0 ($CH_2$), 100.4 (C), 110.9 (CH), 116.4 (C), 122.4 (CH), 135.9 (CH, C-3), 147.6 (C), 161.6 (C), 162.8 (C, C=O) ppm. These NMR data matched previously reported data.[40]

**4.2.13 2-(4-Chlorobenzylidene)malonamide 3m.** A mixture of 4-chlorobenzaldehyde **1a** (141 mg, 1 mmol), malonamide **2b** (102 mg, 1 mmol), and piperidine (10 mol%, 10 μL) in ethanol (3 mL) was stirred at room temperature for 6 h to afford compound **3m** as a white solid (139 mg, 62%). M.p. 202–203 °C (amorphous) (Lit. 189–192 °C).[58] FTIR (ATR): 3372 ($\nu_{as}$ $NH_2$ non-hydrogen bonded), 3310 ($\nu_s$ $NH_2$ non-hydrogen bonded), 3236 ($\nu_{as}$ $NH_2$ hydrogen bonded), 3157 ($\nu_s$ $NH_2$ hydrogen bonded), 3030, 1670 ($\nu$C=O), 1602 ($\nu$C=C), 1492, 1429, 1380, 1331, 1277, 1090, 1014, 827, 679, 646, 625, 617, 500, 430 $cm^{-1}$. $^1H$ NMR (400 MHz, DMSO-$d_6$): 7.24 (br s, 1H), 7.28 (s, 1H), 7.37 (br s, 1H), 7.47 (d, $J$ = 8.8 Hz, 2H), 7.52 (br s, 1H), 7.56 (d, $J$ = 8.8 Hz, 2H), 7.86 (br s, 1H) ppm. $^{13}C\{^1H\}$ NMR (101 MHz, DMSO-$d_6$): 128.7 (2CH), 130.9 (2CH), 132.8 (CH), 133.0 (C), 133.8 (C), 134.1 (C), 165.6 (C, C=O), 168.9 (C, C=O) ppm. These NMR data matched previously reported data.[58]

**4.2.14 2-(4-(Diphenylamino)benzylidene)malonamide 3n.** A mixture of 4-(diphenylamino)benzaldehyde **1f** (273 mg, 1 mmol), malonamide **2b** (102 mg, 1 mmol), and piperidine (10 mol%, 10 μL) in ethanol (3 mL) was stirred at room temperature for 24 h to afford compound **3n** as a yellow solid (193 mg, 54%). M.p. 230 °C (amorphous). FTIR (ATR): 3362 ($\nu_{as}$ $NH_2$ non-hydrogen bonded), 3328 ($\nu_s$ $NH_2$ non-hydrogen bonded), 3248 ($\nu_{as}$ $NH_2$ hydrogen bonded), 3172 ($\nu_s$ $NH_2$ hydrogen bonded), 3060, 1670 ($\nu$C=O), 1579 ($\nu$C=C), 1486, 1326, 1282, 1178, 1073, 922, 832, 759, 693, 654, 606, 593, 529, 507, 487, 450 m $cm^{-1}$. $^1H$ NMR (400 MHz, DMSO-$d_6$): 6.88 (d, $J$ = 8.8 Hz, 2H), 7.03–7.15 (m, 7H), 7.22 (s, 2H), 7.34 (dd, $J$ = 8.0, 8.0 Hz, 4H), 7.43–7.49 (m, 3H), 7.83 (s, 1H) ppm. $^{13}C\{^1H\}$ NMR (101 MHz, DMSO-$d_6$): 121.1 (2CH), 124.0 (2CH), 124.9 (4CH), 127.0 (C), 129.7 (4CH), 130.8 (2CH), 130.9 (C), 133.8 (CH), 146.5 (2C), 148.2 (C), 165.9 (C, C=O), 169.6 (C, C=O) ppm. HRMS (ESI+): $m/z$ calculated for $C_{22}H_{18}N_3O_2^+$ 356.1394 $[M - H_2 + H]^+$; found 356.1398.

**4.2.15 Ethyl (*E*)-2-cyano-3-(4-(diphenylamino)phenyl) acrylate 3o.** A mixture of 4-(diphenylamino)benzaldehyde **1f** (273 mg, 1 mmol), ethyl cyanoacetate **2c** (106 μL, 1 mmol), and piperidine (10 mol%, 10 μL) in ethanol (3 mL) was stirred at room temperature for 24 h to afford compound **3o** as an orange solid (298 mg, 81%). M.p. 96–97 °C (amorphous) (Lit. 118–120 °C).[59] FTIR (ATR): 3060, 3033, 2986, 2902, 2214 ($\nu$C≡N), 1711 ($\nu$C=O), 1569 ($\nu$C=C), 1503, 1484, 1336, 1319, 1265, 1215, 1176, 1091, 1022, 964, 830, 758, 696, 635, 618, 604, 583, 507, 455 $cm^{-1}$. $^1H$ NMR (400 MHz, $CDCl_3$): 1.38 (t, $J$ = 7.0 Hz, 3H), 4.35 (q, $J$ = 7.0 Hz, 2H), 6.98 (d, $J$ = 8.8 Hz, 2H), 7.15–7.22 (m, 6H), 7.35 (t, $J$ = 7.8 Hz, 4H), 7.85 (d, $J$ = 8.8 Hz, 2H), 8.09 (s, 1H, H-3) ppm. $^{13}C\{^1H\}$ NMR (101 MHz, $CDCl_3$): 14.4 ($CH_3$), 62.3 ($CH_2$), 97.4 (C), 116.9 (C), 119.2 (2CH), 123.5 (C), 125.6 (2CH), 126.6 (4CH), 129.9 (4CH), 133.3 (2CH), 145.8 (2C), 152.6 (C), 154.1 (CH, C-3), 163.8 (C, C=O) ppm. These NMR data matched previously reported data.[59]

### 4.3 Synthesis of (*E*)-2-cyano-3-(4-(prop-2-yn-1-yloxy)phenyl) acrylamide 5

A mixture of (*E*)-2-cyano-3-(4-hydroxyphenyl)acrylamide **3i** (188 mg, 1.0 mmol), propargyl bromide solution (80 wt% in toluene, 112 μL, 1.0 mmol) **4a**, and cesium carbonate (326 mg, 1.0 mmol) in *N*,*N*-dimethylformamide (2.0 mL) was stirred at room temperature for 3 h. Upon completion, the reaction mixture was filtered, and the solid residue was washed with ethyl acetate (10 mL). The filtrate was treated with 1.0 M NaOH (2 mL) and extracted with ethyl acetate (3 × 5 mL). The organic layers were combined, washed with brine (2 × 10 mL), dried over anhydrous $Na_2SO_4$, filtered, and concentrated under reduced pressure to obtain the crude product. Purification by flash chromatography on silica gel afforded compound **5** as a white solid (201 mg, 89%). M.p. 165–166 °C (amorphous). FTIR (ATR): 3450 ($\nu_{as}$ $NH_2$ non-hydrogen bonded), 3399 ($\nu_{as}$ $NH_2$

hydrogen bonded), 3310 ($\nu_s$ $NH_2$ non-hydrogen bonded), 3182 ($\nu_s$ $NH_2$ hydrogen bonded), 3090, 2230 ($\nu$C≡N), 1715 ($\nu$C=O), 1608 ($\nu$C=C), 1585 ($\nu$C=C), 1470, 1393, 1144, 1110, 1051, 924, 842, 826, 792, 765, 592, 559, 532, 446 $cm^{-1}$. $^1H$ NMR (400 MHz, DMSO-$d_6$): 3.65 (t, $J = 2.4$ Hz, 1H), 4.92 (d, $J = 2.4$ Hz, 2H), 7.18 (d, $J = 8.8$ Hz, 2H), 7.71 (br s, 1H, $NH_a$), 7.84 (br s, 1H, $NH_b$), 7.97 (d, $J = 8.8$ Hz, 2H), 8.12 (s, 1H, H-3) ppm. $^{13}C\{^1H\}$ NMR (101 MHz, DMSO-$d_6$): 55.8 ($CH_2$), 78.7 (C), 78.9 (CH), 103.5 (C), 115.6 (2CH), 117.1 (C), 125.1 (C), 123.4 (2CH), 150.1 (CH, C-3), 160.4 (C), 163.1 (C, C=O) ppm. HRMS (ESI+): *m/z* calculated for $C_{13}H_{11}N_2O_2^+$ 227.0815 $[M + H]^+$; found 227.0814.

### 4.4 Synthesis of (*E*)-3-(4-((1-benzyl-1*H*-1,2,3-triazol-4-yl) methoxy)phenyl)-2-cyanoacrylamide 6

A mixture of (*E*)-2-cyano-3-(4-(prop-2-yn-1-yloxy)phenyl) acrylamide **5** (113 mg, 0.50 mmol), benzyl bromide **4b** (59 μL, 0.50 mmol), sodium azide (32 mg, 0.50 mmol), and CuI (9.5 mg, 10 mol%) in a 1 : 1 v/v mixture of distilled water and ethanol (2.0 mL) was stirred at 60 °C for 12 h. Upon completion, the resulting solid was filtered, washed with a cold 1 : 1 v/v mixture of distilled water and ethanol (5.0 mL), and dried to afford the 1,4-disubstituted 1,2,3-triazole **6** as a pale yellow solid (142 mg, 79%). M.p. 145–147 °C (amorphous). FTIR (ATR): 3450 ($\nu_{as}$ $NH_2$ non-hydrogen bonded), 3399 ($\nu_{as}$ $NH_2$ hydrogen bonded), 3310 ($\nu_s$ $NH_2$ non-hydrogen bonded), 3182 ($\nu_s$ $NH_2$ hydrogen bonded), 3090, 2230 ($\nu$C≡N), 1715 ($\nu$C=O), 1608 ($\nu$C=C), 1585 ($\nu$C=C), 1470, 1393, 1144, 1110, 1051, 924, 842, 826, 792, 765, 592, 559, 532, 446 $cm^{-1}$. $^1H$ NMR (400 MHz, DMSO-$d_6$): 5.26 (s, 2H), 5.62 (s, 2H), 7.23 (d, $J = 8.4$ Hz, 2H), 7.30–7.40 (m, 5H), 7.71 (br s, 1H, $NH_a$), 7.83 (br s, 1H, $NH_b$), 7.96 (d, $J = 8.4$ Hz, 2H), 8.11 (s, 1H), 8.35 (s, 1H) ppm. $^{13}C\{^1H\}$ NMR (101 MHz, DMSO-$d_6$): 52.9 ($CH_2$), 61.4 ($CH_2$), 103.1 (C), 115.5 (2CH), 117.1 (C), 124.7 (C), 125.1 (CH), 125.1 (C), 128.0 (2CH), 128.2 (CH), 128.8 (2CH), 132.4 (2CH), 136.0 (C), 150.1 (CH, C-3), 161.3 (C), 163.1 (C, C=O) ppm. HRMS (ESI+): *m/z* calculated for $C_{20}H_{18}N_5O_2^+$ 360.1455 $[M + H]^+$; found 360.1452.

### 4.5 Single-crystal X-ray diffraction analysis

X-ray crystallographic analysis was performed at ambient temperature (298 K) using CuKα radiation ($\lambda = 1.54184$ Å) and ω-scan measurements on an Agilent SuperNova diffractometer (Dual source, Cu at Zero configuration) equipped with an Atlas four-circle goniometer and CCD detector. Diffraction frames were processed and integrated with the CrysAlis PRO software suite,[60] and empirical absorption corrections were applied using the SCALE3 ABSPACK scaling algorithm implemented in the same package. The molecular structures of compounds **3i** and **3n** were solved iteratively and completed by Fourier difference mapping.[61] Subsequent refinement of the crystal structure was performed with SHELXL2018/3,[62] and molecular as well as supramolecular graphics were generated with Mercury.[63] Electrostatic potential mapping over the Hirshfeld surface was performed using the CrystalExplorer program.[64] Crystallographic data for compound **3i** have been deposited in the Cambridge Crystallographic Data Center under deposition number CCDC-2483802. Crystallographic data for compound **3n** has been included in the SI due to the low quality of the data.

### 4.6 Anticancer activity

All biological assays, including the handling of reagents and human cancer cell lines, were conducted externally by the National Cancer Institute (NCI, USA) as part of the NCI-60 human tumor cell screening program.[65] All compounds submitted to this program are initially evaluated at a single concentration (10 μM) across the entire panel. The one-dose experiments provide the relative growth of treated cells compared with untreated controls and the initial cell population at time zero. Compounds that display significant growth inhibition in the one-dose screen are subsequently tested at five concentrations in the NCI-60 cell panel.[65]

The human tumor cell lines included in the screening panel are cultured in RPMI-1640 medium supplemented with 5% fetal bovine serum and 2 mM l-glutamine. For each assay, cells are inoculated into 96-well microtiter plates (100 μL per well) at plating densities ranging from 5000 to 40 000 cells per well, depending on the doubling time of each cell line. Following inoculation, the plates are incubated for 24 h at 37 °C in a humidified atmosphere containing 5% $CO_2$ and 95% air prior to the addition of the experimental drugs. After 24 h, two plates of each cell line are fixed *in situ* with trichloroacetic acid (TCA) to determine the cell population at the time of drug addiction ($T_z$). The samples are dissolved in dimethylsulfoxide (DMSO) at 400 times the desired final maximum test concentration and stored frozen until use. At the time of sample addition, an aliquot of the frozen concentrate is thawed and diluted to twice the intended final concentration using complete medium supplemented with 50 μg $mL^{-1}$ gentamicin. An additional four 10-fold or 1/2 log serial dilutions were made to provide a total of five drug concentrations plus the control. Aliquots of 100 μL from each dilution are then added to the appropriate wells already containing 100 μL of medium, resulting in the required final sample concentrations. After the tested compounds were added, the plates are incubated for an additional 48 h at 37 °C in a humidified atmosphere of 5% $CO_2$, 95% air, and 100% relative humidity. For adherent cells, the assay is terminated by the addition of cold trichloroacetic acid (TCA). Cells are fixed *in situ* by the gentle addition of 50 μL of cold 50% (w/v) TCA (final concentration, 10% TCA) and incubated for 60 min at 4 °C. The supernatant is discarded, and the plates are washed five times with tap water and air dried. Sulforhodamine B (SRB) solution (100 μL) at 0.4% (w/v) in 1% acetic acid is added to each well, and the plates are incubated for 10 min at room temperature. After staining, the unbound dye is removed by washing five times with 1% acetic acid, and the plates are air dried. The bound stain is subsequently solubilized with 10 mM trizma base, and the absorbance is measured using an automated plate reader at a wavelength of 515 nm. For suspension cells, the methodology is identical, except that the assay is terminated by fixing the settled cells at the bottom of the wells through the gentle addition of 50 μL of 80% TCA (final concentration, 16% TCA). Using seven absorbance measurements [time zero ($T_z$), control growth ($C$), and test growth in the presence of drug at the five

 

concentration levels ($T_i$)], the percentage growth is calculated at each of the drug concentrations levels. Growth percentage is calculated as: $[(T_i - T_z)/(C - T_z)] \times 100$ for concentrations where $T_i \geq T_z$, and $[(T_i - T_z)/T_z] \times 100$ for concentrations where $T_i < T_z$. Three dose response parameters are calculated for each experimental compound. The 50% growth inhibition ($GI_{50}$) value is determined from the equation $[(T_i - T_z)/(C - T_z)] \times 100 = 50$, corresponding to the drug concentration that produces a 50% reduction in the net protein increase (as measured by SRB staining) relative to the untreated control cells during incubation. The total growth inhibition (TGI) value is defined as the drug concentration at which $T_i = T_z$, indicating complete cessation of cell growth. The 50% lethal concentration ($LC_{50}$) represents the drug concentration that causes a 50% reduction in total cellular protein at the end of treatment compared to the initial value, calculated using the equation $[(T_i - T_z)/T_z] \times 100 = 50$, and reflects a net loss of viable cells. These three parameters are calculated whenever the corresponding activity levels are achieved; if not, or if they exceed the tested range, the results are reported as greater or less than the maximum or minimum concentration evaluated.[65]

### 4.7 Molecular docking

The Knoevenagel adducts **3f**, **3n**, and **3o** were modelled in Discovery Studio 2022 (DS 2022) using standard bond lengths and angles. Their molecular geometries were optimized by energy minimization with the adopted-based Newton-Rapson algorithm until an RMS gradient below 0.01 kcal $mol^{-1}$ $Å^{-2}$ was achieved. The 3D crystal structure of EGFR in complex with Erlotinib (PDB ID: 1M17) was obtained from the RCSB Protein Data Bank. Protein preparation in DS 2022 involved removal of water molecules, heteroatoms, co-crystallized solvents, and ligands. Subsequently, hydrogens and partial charges were added to proteins and ligands using AutoDockTools (ADT version 1.5.7), with Gasteiger charges assigned. Ligands were allowed to adopt flexible conformations during docking. The docking box was generated with ADT, centered within the protein, and defined dimensions of 62 Å × 64 Å × 50 Å and a resolution of 1 Å, centered at coordinates $x = 24.500$, $y = 6.900$, and $z = 58.487$. Docking calculations were performed with AutoDock Vina,[52] and the top-ranked binding pose of the ligands within the EGFR active site were selected for further analysis in Discovery Study (DS).

## Author contributions

CS-S: investigation, methodology; II: computational analysis, writing – original draft; MAM: X-ray crystallographic analysis, writing – original draft; J-CC: conceptualization, methodology, writing – original draft; DB: conceptualization, methodology, writing – original draft.

## Conflicts of interest

There are no conflicts to declare.

## Abbreviations

| | |
|---|---|
| TCIs | Targeted covalent inhibitors |
| TKIs | Tyrosine kinase inhibitors |
| EGFR | Epidermal growth factor receptor |
| NSCLC | Non-small cell lung cancer |
| HER2 | Human epidermal growth factor receptor 2 |
| BTK | Bruton's tyrosine kinase |
| CLL | Chronic lymphocytic leukemia |
| SLL | Small lymphocytic lymphoma |
| FGFR | Fibroblast growth factor receptor |
| JAK3 | Janus kinase 3 |
| PP | Piperidine |
| DBU | 1,8-Diazabicyclo(5.4.0)undec-7-ene |
| BBB | Blood brain barrier |
| TPSA | Topological polar surface area |
| %ABS | Percentage of absorption |
| NCI | National Cancer Institute |
| SRB | Sulforhodamine B |

## Data availability

The data supporting this article are provided in the supplementary information (SI). Supplementary information: IR, NMR, and HRMS spectra, as well as X-ray crystallographic data for compounds reported in this study. See DOI: https://doi.org/10.1039/d5ra07121f.

CCDC 2483802 (**3i**) contains the supplementary crystallographic data for this paper.[66]

## Acknowledgements

The authors acknowledge the financial support provided by the Dirección de Investigaciones at the Universidad Pedagógica y Tecnológica de Colombia (Projects SGI-3724 and SGI-3927). I. I. acknowledges support from the Universidad de Alcalá. M. A. A. gratefully acknowledges support from the Facultad de Ciencias at the Universidad de los Andes. We also extend our sincere gratitude to the National Cancer Institute (NCI) for performing the *in vitro* anticancer assays.

## References

1 F. Sutanto, M. Konstantinidou and A. Dömling, *RSC Med. Chem.*, 2020, **11**, 876–884.
2 W. Lu, M. Kostic, T. Zhang, J. Che, M. P. Patricelli, L. H. Jones, E. T. Chouchaniae and N. S. Gray, *RSC Chem. Biol.*, 2021, **2**, 354–367.
3 L. Boike, N. J. Henning and D. K. Nomura, *Nat. Rev. Drug Discovery*, 2022, **21**, 881–898.
4 K. McAulay, A. Bilsland and M. Bon, *Pharmaceuticals*, 2022, **15**, 1366.
5 L. Arce-Ramos, J.-C. Castillo and D. Becerra, *Pharmaceuticals*, 2023, **16**, 1265.

6 M. Gehringer and S. A. Laufer, *J. Med. Chem.*, 2019, **62**, 5673–5724.
7 N. V. Mehta and M. S. Degani, *Drug Discovery Today*, 2023, **28**, 103799.
8 P. Ábrányi-Balogh and G. M. Keseru, in *Advances in Chemical Proteomics*, ed. X. Yao, Elsevier, Amsterdam, 2022, ch. 2, pp. 47–73.
9 T. A. Baillie, *Expert Opin. Drug Discovery*, 2020, **16**, 275–287.
10 L. Hillebrand, X. J. Liang, R. A. M. Serafim and M. Gehringer, *J. Med. Chem.*, 2024, **67**, 7668–7758.
11 R. Roskoski Jr., *Pharmacol. Res.*, 2024, **200**, 107059.
12 R. Roskoski Jr., *Pharmacol. Res.*, 2025, **216**, 107723.
13 T. Tang, J. Luo, D. Zhang, Y. Lu, W. Liao and J. Zhang, *Eur. J. Med. Chem.*, 2025, **284**, 117202.
14 S. E. Dalton, O. Di Pietro and E. Hennessy, *J. Med. Chem.*, 2025, **13**, 2307–2313.
15 L. Liang, Z. Zhang, Q. You and X. Guo, *Bioorg. Med. Chem.*, 2024, **112**, 117902.
16 Y. Jiang, X. Fang, Y. Xiang, T. Fang, J. Liu and K. Lu, *Curr. Oncol.*, 2023, **30**, 5337–5349.
17 Y. N. Lamb, *Targeted Oncol.*, 2021, **16**, 687–695.
18 J. E. Shin, H. A. Jung, S. Park, J.-M. Sun, S.-H. Lee, J. S. Ahn, M.-J. Ahn and B. Y. Shim, *Sci. Rep.*, 2025, **15**, 4593.
19 N. Gupta, A. Largajolli, H. Witjes, P. M. Diderichsen, S. Zhang, M. J. Hanley, J. Lin and M. Mehta, *Clin. Pharmacol. Ther.*, 2022, **112**, 327–334.
20 H.-L. Jeon, M. Kwak, S. Kim, H.-Y. Yu, J.-Y. Shin and H. A. Jung, *Sci. Rep.*, 2024, **14**, 14659.
21 E. D. Deeks, *Drugs*, 2017, **77**, 1695–1704.
22 K. J. Maddocks, A. S. Ruppert, G. Lozanski, N. A Heerema, W. Zhao, L. Abruzzo, A. Lozanski, M. Davis, A. Gordon, L. L. Smith, R. Mantel, J. A. Jones, J. M. Flynn, S. M. Jaglowski, L. A. Andritsos, F. Awan, K. A. Blum, M. R. Grever, A. J. Johnson, J. C. Byrd and J. A. Woyach, *JAMA Oncol.*, 2015, **1**, 80–87.
23 A. Markham and S. Dhillon, *Drugs*, 2018, **78**, 139–145.
24 C. S. Tam, J. L. Muñoz, J. F. Seymour and S. Opat, *Blood Cancer J.*, 2023, **13**, 141.
25 M. Javle, G. King, K. Spencer and M. J. Borad, *Oncologist*, 2023, **28**, 928–943.
26 B. King, J. Soung, C. Tziotzios, L. Rudnicka, P. Joly, M. Gooderham, R. Sinclair, N. A. Mesinkovska, C. Paul, Y. Gong, S. D. Anway, H. Tran, R. Wolk, S. H. Zwillich and A. Lejeune, *Am. J. Clin. Dermatol.*, 2024, **25**, 299–314.
27 I. M Serafimova, M. A. Pufall, S. Krishnan, K. Duda, M. S. Cohen, R. L. Maglathlin, J. M. McFarland, R. M. Miller, M. Frödin and J. Taunton, *Nat. Chem. Biol.*, 2012, **8**, 471–476.
28 T. D. Owens, K. A. Brameld, E. J. Verner, T. Ton, X. Li, J. Zhu, M. R. Masjedizadeh, J. M. Bradshaw, R. J. Hill, D. Tam, A. Bisconte, E. O. Kim, M. Francesco, Y. Xing, J. Shu, D. Karr, J. LaStant, D. Finkle, N. Loewenstein, H. Haberstock-Debic, M. J. Taylor, P. Nunn, C. L. Langrish and D. M. Goldstein, *J. Med. Chem.*, 2022, **65**, 5300–5316.
29 M. Forster, A. Chaikuad, S. M. Bauer, J. Holstein, M. B. Robers, C. R. Corona, M. Gehringer, E. Pfaffenrot, K. Ghoreschi, S. Knapp and S. A. Laufer, *Cell Chem. Biol.*, 2016, **23**, 1335–1340.
30 S. Johari, M. R. Johan and N. G. Khaligh, *Org. Biomol. Chem.*, 2022, **20**, 2164–2186.
31 J. N. Appaturi, R. Ratti, B. L. Phoon, S. M. Batagarawa, I. U. Din, M. Selvaraj and R. J. Ramalingam, *Dalton Trans.*, 2021, **50**, 4445–4469.
32 C. Serrano-Sterling, D. Becerra, J. Portilla, H. Rojas, M. Macías and J.-C. Castillo, *J. Mol. Struct.*, 2021, **1244**, 130944.
33 J. Stec and W. H. Witola, *Results Chem.*, 2023, **6**, 101212.
34 C. Nitsche, C. Steuer and C. D. Klein, *Bioorg. Med. Chem.*, 2011, **19**, 7318–7337.
35 K. M. Uddin, M. H. Meem, M. Akter, S. Rahman, M. A. Al-Gawati, N. Alarifi, H. Albrithen, A. Alodhayb, R. A. Poirier and M. H. Bhuiyan, *MethodsX*, 2024, **12**, 102691.
36 D. E. Quintero Jimenez, L. Lima Zanin, L. Farinelli Diniz, J. Ellena and A. L. Meleiro Porto, *Curr. Microwave Chem.*, 2019, **6**, 54–60.
37 T. R. Burke, B. Lim, V. E. Marquez, Z.-H. Li, J. B. Bolen, I. Stefanova and I. D. Horak, *J. Med. Chem.*, 1993, **36**, 425–432.
38 S. Son, H. Kim, H. Y. Yun, D. H. Kim, S. Ullah, S. J. Kim, Y.-J. Kim, M.-S. Kim, J.-W. Yoo, P. Chun and H. R. Moon, *Bioorg. Med. Chem.*, 2015, **23**, 7728–7734.
39 F. Pandolfi, M. Feroci and I. Chiarotto, *ChemistrySelect*, 2018, **3**, 4745–4749.
40 E. Y. Mesa Castro, A. F. Monroy Ramírez, J. J. Martínez, J.-C. Castillo and G. A. Caicedo Pineda, *Catalysts*, 2024, **14**, 927.
41 S. Mancipe, J.-C. Castillo, M. H. Brijaldo, V. P. López, H. Rojas, M. A. Macías, J. Portilla, G. P. Romanelli, J. J. Martínez and R. Luque, *ACS Sustainable Chem. Eng.*, 2022, **10**, 12602–12612.
42 K.-D. Wu, G. S. Chen, J.-R. Liu, C.-E. Hsieh and J.-W. Chern, *ACS Med. Chem. Lett.*, 2019, **10**, 22–26.
43 A. Tigreros, M.-C. Ríos, C. Serrano-Sterling, D. Becerra, J.-C. Castillo and J. Portilla, *J. Mol. Struct.*, 2025, **1321**, 139926.
44 A. C. Lipinski, *Drug Discovery Today: Technol.*, 2004, **1**, 337–341.
45 S. Prasanna and R. J. Doerksen, *Curr. Med. Chem.*, 2009, **16**, 21–41.
46 M. Bitew, T. Desalegn, T. B. Demissie, A. Belayneh, M. Endale and R. Eswaramoorthy, *PLoS One*, 2021, **16**, e0260853.
47 W. Wei, S. Cherukupalli, L. Jing, X. Liu and P. Zhan, *Drug Discovery Today*, 2020, **25**, 1839–1845.
48 National Cancer Institute, *DCTD Division of Cancer Treatment & Diagnosis*, available online: https://dtp.cancer.gov/discovery_development/nci-60/methodology.htm, accessed on 15 July 2025.
49 L. M. Moreno, J. Quiroga, R. Abonia, A. Lauria, A. Martorana, H. Insuasty and B. Insuasty, *RSC Adv.*, 2020, **10**, 34114.
50 N. Khurana and S. C. Sikka, *Cancers*, 2018, **10**, 352.
51 F. A. Verza, G. C. Da Silva and F. G. Nishimura, *Oncol. Res.*, 2025, **33**, 1819–1834.

52 P. A. Morese, A. Ahmad, M. P. Martin, R. A. Noble, S. Pintar, L. Z. Wang, S. Xu, A. Lister, R. A. Ward, A. K. Bronowska, M. E. M. Noble, H. L. Stewart and M. J. Waring, *Commun. Chem.*, 2025, **8**, 111.
53 D. N. do Amaral, J. Lategahn, H. H. Fokoue, E. M. B. da Silva, C. M. R. Sant'Anna, D. Rauh, E. J. Barreiro, S. Laufer and L. M. Lima, *Sci. Rep.*, 2019, **9**, 14.
54 O. Trott and A. J. Olson, *J. Comput. Chem.*, 2010, **31**, 455–461.
55 R. Gunasekar, P. Thamaraiselvi, R. S. Rathore, K. I. Sathiyanarayanan and S. Easwaramoorthi, *J. Org. Chem.*, 2015, **80**, 12351–12358.
56 B. D. Rupanwar, S. S. Chavan, A. M. Shelkea and G. M. Suryavanshi, *New J. Chem.*, 2018, **42**, 6433–6440.
57 M. Curini, F. Epifano, M. C. Marcotullio, O. Rosati and A. Tsadjout, *Synth. Commun.*, 2002, **32**, 355–362.
58 C. N. O'Callaghan and T. B. H. McMurry, *J. Chem. Res.*, 1989, **6**, 1219–1231.
59 P. S. Hariharan, V. K. Prasad, S. Nandi, A. Anoop, D. Moon and S. P. Anthony, *Cryst. Growth Des.*, 2017, **17**, 146–155.
60 *CrysAlisPro 1.171.39.46e*, Rigaku Oxford Diffraction, 2018.
61 L. Palatinus and G. Chapuis, *J. Appl. Crystallogr.*, 2007, **40**, 786–790.
62 G. M. Sheldrick, *Acta Crystallogr., Sect. C:Struct. Chem.*, 2015, **71**, 3–8.
63 C. F. Macrae, I. J. Bruno, J. A. Chisholm, P. R. Edgington, P. McCabe, E. Pidcock, L. Rodriguez-Monge, R. Taylor, J. van de Streek and P. A. Wood, *J. Appl. Crystallogr.*, 2008, **41**, 466–470.
64 M. J. Turner, J. J. McKinnon, S. K. Wolff, D. J. Grimwood, P. R. Spackman, D. Jayatilaka and M. A. Spackman, *CrystalExplorer17*, University of Western Australia, 2017.
65 *NCI-60 Screening Methodology*, https://dctd.cancer.gov/drug-discovery-development/assays/high-throughput-screening-services/nci60/submitting-compounds/screening-methodology.pdf, accessed November 4, 2025.
66 CCDC 2483802: Experimental Crystal Structure Determination, 2025, DOI: 10.5517/ccdc.csd.cc2pclnb.